

# Dissipative advective accretion disc solutions with variable adiabatic index around black holes

Rajiv Kumar<sup>1</sup>, Indranil Chattopadhyay<sup>1\*</sup>

<sup>1</sup> *Aryabhata Research Institute of Observational Sciences (ARIES), Manora Peak, Nainital-263002, India*

## ABSTRACT

We investigated accretion on to black holes in presence of viscosity and cooling, by employing an equation of state with variable adiabatic index and multi-species fluid. We obtained the expression of generalized Bernoulli parameter which is a constant of motion for an accretion flow in presence of viscosity and cooling. We obtained all possible transonic solutions for a variety of boundary conditions, viscosity parameters and accretion rates. We identified the solutions with their positions in the parameter space of generalized Bernoulli parameter and the angular momentum on the horizon. We showed that a shocked solution is more luminous than a shock-free one. For particular energies and viscosity parameters, we obtained accretion disc luminosities in the range of  $10^{-4} - 1.2$  times Eddington limit, and the radiative efficiency seemed to increase with the mass accretion rate too. We found steady state shock solutions even for high-viscosity parameters, high accretion rates, and for wide range of composition of the flow, starting from purely electron-proton to lepton-dominated accretion flow. However, similar to earlier studies of inviscid flow, accretion shock was not obtained for electron-positron pair plasma.

**Key words:** accretion, accretion disc - black hole physics - Hydrodynamics - Radiation mechanism: general - shock waves.

\* E-mail: rajiv.k@aries.res.in (RK); indra@aries.res.in (IC)

## 1 INTRODUCTION

Observations of electromagnetic spectra and mass outflow in the form of jets from microquasars and active galactic nuclei (AGN) are better explained as a consequence of conversion of gravitational energy released from matter falling into extreme compact objects like black holes. AGN are supposed to harbour  $10^{6-9} M_{\odot}$  (where,  $M_{\odot}$  is solar mass) black holes at the centre, and microquasars harbour black holes of mass  $\sim 10 M_{\odot}$  at the centre. Microquasars moves from a ‘low hard spectral state’ (LHS) *i.e.*, when the accretion disc is radiatively inefficient and the electro-magnetic power maximizes in the higher energy power-law tail, to the ‘high soft spectral state’ (HSS) *i.e.*, when the disc is radiatively efficient and the power maximizes in the lower, thermal part of the spectra (Remillard & McClintock 2006). These two states are connected by a series of intermediate states. In fact, the time-scales in microquasars and AGN scale with the mass of the central object (McHardy et. al. 2006), and shows that the basic physics close to the horizon is similar. As a result, timing properties can be studied by observing the microquasars which are much faster varying than the AGN. In particular, since the time-scales are large, AGN generally do not show state transition, therefore, a closer look at the timing properties of microquasars may shed some light on when the transitions are expected for AGN. Microquasars also show quasi-periodic oscillation (QPOs) in the hard power law photons (Remillard & McClintock 2006), and in the outbursting sources, the QPO frequency grows with the luminosity and as the spectral state moves from LHS to the intermediate states (Shapashnikov & Titarchuk 2009; Nandi *et al.* 2012). Moreover, black hole candidates (BHCs) are associated with bipolar jets (Biretta 1993; Mirabel & Rodriguez 1994). Since black holes have no atmosphere, therefore, jets have to originate from the accretion disc. Observations also suggest that these jets originate within a few tens of Schwarzschild radii ( $r_g$ ) from the horizon (Junor et. al. 1999; Doeleman et. al. 2012). Although from centres of galaxies jets have been observed either to exist or none at all, however, microquasars jets have been observed to evolve with the change in its spectral state (Gallo et. al. 2003). In other words, if we accept the conclusions of McHardy et. al. (2006), then those centres of galaxies which harbours central black holes but do not exhibit the presence of jet, should start generating jets as and when the state of the accretion disc changes to jet generating mode, and vice versa. Since accretion is the main driver that fuels AGN and microquasars, so it is very important to understand the accretion physics in details.

It is well known that matter enters the black hole with the speed of light or  $c$  (Weinberg 1972), and at large distances away from the horizon should have negligible infall velocity, therefore, matter accreting on to black holes are necessarily transonic, or in other words, matter falling on to a black hole makes a subsonic to supersonic transition. Moreover, the presence of marginally stable orbit ensures that matter entering a black hole must have sub-Keplerian angular momentum. These features are imposed by the inner boundary condition of the space-time geometry around the black hole. It implies that black hole accretion should have significant advection. The very first model for accretion on to black holes is the general relativistic version of Bondi flow (Bondi 1952; Michel 1972), which satisfies all the above properties of black hole accretion. But this model could not explain observed luminosities around BHCs, since Bondi flow is a radial flow whose infall time-scale is too small to produce the luminosities observed (Shapiro 1973). To circumvent this problem, the Keplerian disc or Shakura-Sunyaev (SS) standard disc model was proposed by Shakura & Sunyaev (1973); Novikov & Thorne (1973). In this model, the disc matter is rotation dominated with Keplerian angular momentum distribution and negligible infall velocity. The matter is optically thick, geometrically thin and was successful in explaining thermal multicoloured blackbody part of the spectrum but could not produce non-thermal part of the spectrum. It was shown that a Comptonizing cloud of hot electrons or some kind of a ‘corona’ is required to produce the high-energy non-thermal photons (Sunyaev & Titarchuk 1980). The differences in these models arise due to the importance assigned to the various terms in equations of motion. For Bondi flow, no rotation was considered, and instead of energy equation polytropic equation of state (EoS) was assumed. For SS disc the advection term and the pressure gradient term in the momentum balance equation were ignored, and the heat generated by the viscous disc was assumed to be efficiently radiated away. Although Bondi flow failed as a viable accretion model to explain the luminosities of BHCs, but the unique inner boundary condition of a space-time around a black hole would ensure the nature of accretion solutions close to the horizon to be quasi-Bondi type *i.e.*, advection would be dominant close to the horizon. As a result, accretion models with significant advection gained popularity. Narayan *et al.* (1997) developed a class of solutions called advection-dominated accretion flow (ADAF), characterized by rotating flow with viscous dissipation, and becomes transonic close to the horizon. It was also shown that such flow becomes self-similar at large distances away from the horizon. ADAF got unprecedented popularity as the disc model to explain the observation. However, earlier Liang & Thompson (1980) showed that rotating transonic flow in the

inviscid limit may harbour multiple sonic points. Such accreting flows may undergo transient or steady shock transitions (Fukue 1987; Chakrabarti 1989; Molteni *et al.* 1994, 1996a,b). Presence of multiple sonic point and shocks has been shown to exist for dissipative accretion flows as well (Chakrabarti 1996; Lanzafame *et al.* 1998; Chattopadhyay & Das 2007; Das 2007; Das & Chattopadhyay 2008; Lanzafame *et al.* 2008; Lee *et al.* 2011). Whether an accretion flow is smooth or shocked depends on the outer boundary condition, and ADAF-type solution has been shown to be a subset of general advective, viscous solutions (Lu *et al.* 1999; Becker *et al.* 2008; Kumar & Chattopadhyay 2013; Kumar *et al.* 2014). A shocked solution has a number of advantages. The extra thermal gradient force in the post-shock flow can drive bipolar outflows (Molteni *et al.* 1996b; Lanzafame *et al.* 1998; Das *et al.* 2001; Chattopadhyay & Das 2007; Kumar & Chattopadhyay 2013; Kumar *et al.* 2014), and since shocks occur typically at few tens of  $r_g$ , a shocked disc naturally satisfies the observational criteria that jets are launched closer to the horizon, and the entire disc do not participate in the formation of jets. Moreover, Kumar *et al.* (2014) showed that jets from post-shock disc becomes stronger as the spectral state moves from LHS to hard intermediate spectral states as is observed in microquasars.

Taking clue from the solutions of shocked disc, Chakrabarti & Titarchuk (1995) in a model solution considered Keplerian flow along the equatorial plane and sub-Keplerian flow which flanks the Keplerian disc from above and below. The sub-Keplerian flow may harbour shock, and the post-shock flow being hot and puffed up will intercept a portion of the pre-shock disc photons and inverse-Comptonize them to produce the hard power-law tail, producing the LHS. Very weak shock or no shock means lack of hot electrons, and therefore cannot produce the hard power-law tail, *i.e.*, forms the HSS. Surge in Keplerian accretion rate or the sub-Keplerian accretion rate can be either due to actual supply at the outer boundary, or by redistribution between Keplerian and sub-Keplerian matter due to the change in microphysics which results in a change in viscosity parameter. Evidence of Keplerian and sub-Keplerian matter has been confirmed observationally about a decade ago (Smith *et al.* 2001, 2002, 2007), and recently numerical simulations have confirmed the two-component paradigm (Giri & Chakrabarti 2013). Since post-shock disc is the seat of hard radiation, so oscillating shocks (Molteni *et al.* 1996a; Lanzafame *et al.* 2008; Nagakura & Yamada 2009; Lee *et al.* 2011; Das *et al.* 2014) will induce oscillations in hard radiations as well. Hence, this could naturally explain the QPO. Therefore, entire advective regime which gives rise to

smooth and shocked solutions can qualitatively explain three broad observational features from BHCs like spectral states and its transition, jets, evolution of QPOs.

Most of the above work has been done with fixed adiabatic index ( $\Gamma$ ) EoS. Since accretion flow at very large distance from the black hole is thermally non-relativistic, *i.e.*,  $\Theta (= kT/m_e c^2) < 1$ , and close to it becomes relativistic or  $\Theta \gg 1$ , therefore,  $\Gamma$  should not be a fixed quantity in the flow but depend on temperature. In the definition of  $\Theta$ ,  $k$  is the Boltzmann constant,  $T$  is the temperature and  $m_e$  is electron rest mass. In fact, Taub (1948) showed that a fixed  $\Gamma$  EoS should not be used to obtain solutions of flow which covers non-relativistic to relativistic temperature ranges. Blumenthal & Mathews (1976) presented the first accretion solution using temperature-dependent  $\Gamma$  EoS around black holes. Fukue (1987) showed the presence of accretion shock for a flow composed of electrons and protons ( $e^- - p^+$ ). Chattopadhyay (2008) and Chattopadhyay & Ryu (2009) showed that flow solutions around a black hole depend on the composition of the flow, and that the steady state accretion solutions of electron-positron pair plasma ( $e^- - e^+$ ) possesses flows with non-relativistic temperatures, and as a consequence, do not form accretion shocks (Chattopadhyay 2008; Chattopadhyay & Chakrabarti 2011). Since the relativistic nature of EoS depends on the competition between rest energy and the thermal energy of the flow, so it was found out that a flow becomes thermally the most relativistic if its proton proportion is 25 – 27% of its electron number density (Chattopadhyay & Ryu 2009; Chattopadhyay *et al.* 2012). And the maximum proportion of bipolar outflow is generated when the composition parameter is in this range (Kumar *et al.* 2013). Although accretion solutions with variable  $\Gamma$  EoS around compact objects were obtained before, but as far as we are aware, solutions of rotating, transonic flow with variable  $\Gamma$  EoS which are composed of baryons and leptons in presence of general heating and cooling have not been attempted before. Since the thermal state of the flow and its advective properties ultimately determine the radiative power output, the present attempt is important. Moreover, it would also be important to determine the effect of accretion rate in shaping the nature of solutions and the luminosities generated from such solutions. All these issues will be discussed in the subsequent sections.

In the next section, we introduce the governing equations and outline the assumptions, and, we describe the solution procedure. In Section 3, we present the results, and finally in Section 4, we present the discussion and concluding remarks.

## 2 ASSUMPTIONS AND EQUATIONS OF MOTION

We consider stationary, viscous, rotating and axisymmetric accretion disc around a Schwarzschild black hole. For mathematical simplicity, space-time around the black hole is described by the Paczyński-Wiita (PW) pseudo-Newtonian potential (Paczyński & Wiita 1980). PW potential simplifies our calculations while retaining all the essential qualitative features of strong gravity, and it is easier to incorporate more complicated physics in the pseudo-Newtonian scheme.

### 2.1 Equations of motion

The EoS of a multispecies flow is given by (Chattopadhyay 2008; Chattopadhyay & Ryu 2009)

$$\bar{e} = n_{e-} m_{e-} c^2 f = \rho_{e-} c^2 f = \frac{\rho c^2 f}{K}, \text{ where } K = [2 - \xi(1 - 1/\eta)] \quad (1)$$

and,

$$f = (2 - \xi) \left[ 1 + \Theta \left( \frac{9\Theta + 3}{3\Theta + 2} \right) \right] + \xi \left[ \frac{1}{\eta} + \Theta \left( \frac{9\Theta + 3/\eta}{3\Theta + 2/\eta} \right) \right].$$

Here  $\xi = n_{p+}/n_{e-}$  is the ratio of proton to electron number density, and the ratio of electron to proton mass is given by  $\eta = m_{e-}/m_{p+}$ . The approximate form of EoS of each species of the flow which follows a relativistic Maxwellian distribution was proposed by Ryu *et al.* (2006). Following a different approach, variable  $\Gamma$  was considered for accretion discs by assuming thermal equilibrium between radiation and accreting flow (Mukhopadhyay & Dutta 2012), but in our case no such assumption is required. The charge neutrality is maintained by positron number density  $n_{e+}$ , so  $n_{e-} = n_{p+} + n_{e+}$ . The enthalpy is given by

$$h = \frac{(\bar{e} + p)}{\rho} = \frac{f}{K} + \frac{2\Theta}{K}. \quad (2)$$

where,  $p = 2n_{e-}kT$  is the isotropic gas pressure,  $T$  being the local temperature, and  $\Theta = kT/(m_{e-}c^2)$  is the ratio of thermal energy and the rest energy of the electron. The expression of polytropic index and adiabatic index is given by

$$N = \frac{1}{2} \frac{df}{d\Theta}; \quad \Gamma = 1 + \frac{1}{N} \quad (3)$$

We now employ the units of length, time and velocity as  $r_g = 2GM/c^2$ ,  $r_g/c = 2GM/c^3$  and  $c$ , respectively, where  $M$  is the mass of the black hole is the unit of mass, and  $G$  is the gravitational constant. In the rest of the paper, all the variables and equations are expressed in the above-mentioned unit system. We now present steady state equations of motion in the

advective domain and in presence of viscosity and cooling processes. The radial component of momentum balance equation is given by

$$\vartheta \frac{d\vartheta}{dx} + \frac{1}{\rho} \frac{dp}{dx} - \frac{\lambda^2}{x^3} + \frac{1}{2(x-1)^2} = 0. \quad (4)$$

Here  $\lambda$ ,  $\vartheta$ , and  $x$  are the specific angular momentum, the radial bulk velocity, and the radial coordinate in the units described above. The azimuthal component of momentum balance equation or, angular momentum distribution equation is given by,

$$\frac{d\lambda}{dx} + \frac{1}{\Sigma \vartheta x} \frac{d(x^2 W_{x\phi})}{dx} = 0, \quad (5)$$

The viscous stress is given by  $W_{x\phi} = \varpi x \frac{d\Omega}{dx}$ , and the dynamical viscosity parameter  $\varpi = \Sigma \nu = \rho H (\alpha a^2) / (\Gamma \Omega_K)$ , where,  $\nu$ ,  $\alpha$  and  $\Omega_K$  are the kinematic viscosity parameter, Shakura-Sunyaev viscosity parameter and the Keplerian angular velocity, respectively. The mass conservation equation is given by,

$$\dot{M} = 2\pi \Sigma \vartheta x, \quad (6)$$

where,  $\Sigma = 2\rho H$  is vertically integrated density of the flow. The disc matter is in hydrostatic equilibrium in the vertical direction, the half height of the disc is given by

$$H = 2\sqrt{\frac{\Theta x}{K}}(x-1). \quad (7)$$

The entropy generation equation or the first law of thermodynamics is given by

$$\Sigma \vartheta \left[ \frac{de}{dx} - \frac{p}{\rho^2} \frac{d\rho}{dx} + \frac{Q^+}{\vartheta} - \frac{Q^-}{\vartheta} \right] = 0, \quad (8)$$

where  $e = \bar{e}/\rho = f/K$  is specific energy density of the flow. Here,  $Q^\pm$  are the viscous heating and the total cooling, respectively. Here  $Q^+ = \frac{W_{x\phi}^2}{\eta \Sigma}$  and  $Q^- = \Lambda^-/\Sigma$ . The cooling term is given by  $Q^- = \chi \mathcal{F}(x_s)(Q_S^- + Q_B^-)$ , where  $\chi$  is the cooling parameter, such that the cooling will be turned off by putting  $\chi = 0$ , or will be turned on if  $\chi = 1$ . Here,  $\mathcal{F}(x_s)$  is the Comptonization parameter fitting function, which is calculated once the accretion shock is obtained and has been presented recently by Kumar *et al.* (2014). We assume  $\mathcal{F}(x_s)$  to be generic. The form of this analytical function is given by

$$\mathcal{F}(x_s) = 0.659234 + 0.127851x_s - 0.00043x_s^2 - 1.13 \times 10^{-6}x_s^3, \quad (9)$$

where,  $x_s$  is the location of shock, and  $\mathcal{F}(x_s) \sim 1$  when stable shock solution is not found. The cooling term also contains synchrotron emissivity or  $\Lambda_S^-$  (Shapiro & Teukolsky 1983), and bremsstrahlung emissivity or  $\Lambda_B^-$  (Rybicki & Lightman 1979; Svensson 1982) and are defined as

$$Q_S^- = \Lambda_S^-/\Sigma = \frac{S_0\Theta_e^3}{\vartheta\sqrt{\Theta x^3}(x-1)} \quad \text{and} \quad Q_B^- = \Lambda_B^-/\Sigma = \frac{B_0\sqrt{\Theta_e}}{\vartheta\sqrt{\Theta x^3}(x-1)}, \quad (10)$$

where,

$$S_0 = \frac{16 \times 1.44 \times 10^{17}}{3} \frac{e^4 \beta \dot{m}}{m_e^3 c^3 K^{3/2}} \frac{1}{GM_\odot}$$

and

$$B_0 = \frac{1.44 \times 10^{17} K_{\text{ep}} \xi (2 - \xi) \dot{m}}{16\pi m_e^2 K^{3/2}} \frac{1}{GM_\odot c^2}$$

where  $K_{\text{ep}} = 32m_e c^3 r_e^2 \alpha_f \sqrt{(2/\pi)}/3 = 1.2135 \times 10^{-22}$ ,  $\dot{m} = \dot{M}/\dot{M}_{\text{Edd}}$  is the accretion rate in units of Eddington rate, the fine structure constant is given by  $\alpha_f = 1/137.036$  and classical electron radius  $r_e = 2.81794 \times 10^{-13}$  cm. Here we have considered  $\dot{M}_{\text{Edd}} = 1.44 \times 10^{17} M/M_\odot$ . The magnetic field is stochastic and is assumed to be in total or partial equipartition with the gas pressure. The ratio between magnetic and gas pressure is  $\beta = B^2/(8\pi p)$ , such that  $0 \leq \beta \leq 1$ .

Integrating equation (4) with the help of eqs. (5 — 8), we get

$$\varepsilon = \frac{\vartheta^2}{2} + h - \frac{\lambda^2}{2x^2} + \frac{\lambda\lambda_0}{x^2} - \zeta - \frac{1}{2(x-1)}, \quad (11)$$

where  $\zeta = \int \frac{\Lambda^-}{\Sigma \vartheta} dx = \chi \int \mathcal{F}(x_s) \left( (\Lambda_S^-)/(\Sigma \vartheta) + (\Lambda_B^-)/(\Sigma \vartheta) \right) dx = \zeta_S + \zeta_B$ . Here  $\varepsilon$  is a constant of motion in presence of viscosity and cooling, and we call it the generalized Bernoulli constant, and is also the specific energy of the flow. If we ignore cooling processes in the equation (8) then integral form of equations (4), (5) — (8) becomes

$$E = \frac{\vartheta^2}{2} + h - \frac{\lambda^2}{2x^2} + \frac{\lambda\lambda_0}{x^2} - \frac{1}{2(x-1)}. \quad (12)$$

This is known as grand specific energy (Gu & Lu 2004; Kumar & Chattopadhyay 2013) and is a constant of motion in presence of viscosity but not in presence of cooling. And for non-dissipative flow  $\varepsilon \rightarrow \mathcal{E} = 0.5\vartheta^2 + h + \lambda^2/(2x^2) - 0.5/(x-1)$  which is the canonical definition of Bernoulli parameter.

Integrating equation (8) by putting  $Q^+ = Q^- = 0$ , we get

$$\rho = \mathcal{K} \exp(k_3) \Theta^{3/2} (3\Theta + 2)^{k_1} (3\Theta + 2/\eta)^{k_2}, \quad (13)$$

where,  $k_1 = 3(2 - \xi)/4$ ,  $k_2 = 3\xi/4$ , and  $k_3 = (f - K)/(2\Theta)$ . This is the adiabatic EoS for multispecies fluids (Kumar *et al.* 2013) and  $\mathcal{K}$  is the constant of entropy. Using equations (6) and (13), we can define entropy-accretion rate ( $\dot{\mathcal{M}}$ ) as

$$\dot{\mathcal{M}} = \frac{\dot{M}}{4\pi\mathcal{K}} = \vartheta H x \exp(k_3) \Theta^{3/2} (3\Theta + 2)^{k_1} (3\Theta + 2/\eta)^{k_2}, \quad (14)$$

where  $\dot{\mathcal{M}}$  is also constant for inviscid multispecies relativistic flows.



Integrating equation (5) with the help of equation (6) and using expression of  $W_{x\phi}$ , we get

$$\frac{d\Omega}{dx} = -\frac{\Gamma\vartheta\Omega_K(\lambda - \lambda_0)}{\alpha a^2 x^2}, \quad (15)$$

where,  $\lambda_0$  is the specific angular momentum at the horizon obtained by considering vanishing torque at the event horizon (Weinberg 1972) and  $\Omega_K^2(x) = 1/(2x(x-1)^2)$ . Since  $\lambda = x^2\Omega$ , derivative of  $\lambda$  with respect to  $x$  is written as

$$\frac{d\lambda}{dx} = 2x\Omega + x^2 \frac{d\Omega}{dx}. \quad (16)$$

Using equations (6) and (7) in equation (8), we get

$$\frac{d\Theta}{dx} = -\frac{2\Theta}{2N+1} \left[ \frac{1}{\vartheta} \frac{d\vartheta}{dx} + \frac{5x-3}{2x(x-1)} \right] - \frac{\nu x^2 K}{(2N+1)\vartheta} \left( \frac{d\Omega}{dx} \right)^2 + \frac{K\mathcal{F}(x_s)}{(2N+1)\vartheta} [Q_S^- + Q_B^-]. \quad (17)$$

Using equations (2) and (17) in equation (4), we get

$$\frac{d\vartheta}{dx} = \frac{a^2 \left[ \frac{2N}{2N+1} \frac{5x-3}{2x(x-1)} \right] + \frac{\nu x^2}{\vartheta(2N+1)} \left( \frac{d\Omega}{dx} \right)^2 - \frac{\mathcal{F}(x_s)}{\vartheta(2N+1)} [Q_S^- + Q_B^-] + \frac{\lambda^2}{x^3} - \frac{1}{2(x-1)^2}}{\vartheta - \frac{a^2}{\vartheta} \left[ \frac{2N}{2N+1} \right]}, \quad (18)$$

where,  $a$  is the adiabatic sound speed and is defined as  $a^2 = 2\Theta\Gamma/K$ . To find a complete set of solution we have to integrate eqs. (16–18), with the help of equation (15). These equations are solved by specifying the flow parameters, namely,  $\varepsilon$ ,  $\lambda_0$ ,  $\alpha$  and  $\dot{m}$ . In addition, the lack of knowledge of the exact nature of black hole magnetosphere, influences us to assume the value of  $\beta$  to evaluate  $Q_S^-$ . In the case of black hole accretion, the presence of horizon imposes at least one sonic or critical point ( $x_c$ ). Although, eqs. (16)–(18) can be solved once the flow parameters are supplied, but for dissipative flow the location of  $x_c$  or the number of  $x_{cS}$ , is not known a priori.

### 2.1.1 Critical point conditions

Since accretion on to a black hole is transonic, therefore, at some point the denominator  $\mathcal{D}$  of equation (18) becomes zero, and to maintain the well behaved nature of  $d\vartheta/dx$  the numerator  $\mathcal{N}$  also goes to zero. This point where  $d\vartheta/dx = \mathcal{N}/\mathcal{D} \rightarrow 0/0$  is called the critical point or the sonic point ( $x_c$ ) of the flow. This also gives us the critical point condition,

$$M_c^2 = \frac{\vartheta_c^2}{a_c^2} = \frac{2}{\Gamma_c + 1} \quad (19)$$

and

$$\left[ \frac{(5x_c - 3)M_c^2}{2x_c(x_c - 1)} \right] a_c^2 + \frac{\Gamma_c M_c \Omega_K (\lambda_c - \lambda_0)^2}{\alpha a_c x_c^2 (2N_c + 1)} - \frac{\mathcal{F}(x_s) [Q_{S_c}^- + Q_{B_c}^-]}{\vartheta_c (2N_c + 1)} + \frac{\lambda_c^2}{x_c^3} - \frac{1}{2(x_c - 1)^2} = 0, \quad (20)$$

where  $M_c$ ,  $\vartheta_c$ ,  $a_c$ ,  $\Gamma_c$ ,  $N_c$ , and  $\lambda_c$  are the Mach number, the bulk velocity, the sound speed, the adiabatic index, the polytropic index and the specific angular momentum at the critical point  $x_c$ , respectively. The bulk velocity gradient at the critical point is calculated by l'Hospital rule and is given by

$$\left(\frac{d\vartheta}{dx}\right)_c = \left(\frac{d\mathcal{N}/dx}{d\mathcal{D}/dx}\right)_{x=x_c}. \quad (21)$$

Equations (19–21) give the analytical critical point conditions, which are used to obtain the critical point of the flow.

### 2.1.2 Shock conditions

In the domain of multiple sonic points, supersonic matter through outer sonic point, may be slowed down due to the centrifugal barrier at  $x \lesssim \text{few} \times 10 r_g$ . This may act as a barrier to the supersonic matter following the slowed down matter. If the barrier is strong enough it may produce a centrifugal barrier mediated shock transition. The shock conditions are obtained from conservation of mass, momentum and energy fluxes across the discontinuity (Landau & Lifshitz 1959). The general, compact, and conserved form of the fluid equations are,

$$\partial_t(q) + \partial_x(F_q) = 0,$$

where,  $q$ s are the conserved quantities and  $F_q$  are corresponding fluxes. We now impose the conditions that  $v_z = 0$  and  $\partial/\partial\phi = \partial/\partial z = 0$ , and only the  $x - \phi$  component of the viscous stress is the most dominant. Assuming hydrostatic balance in the vertical direction we obtain the integrated form of the mass flux ( $F_{\text{mass}}$ ), the radial momentum flux ( $F_{x-\text{mom}}$ ), the azimuthal momentum flux ( $F_{\phi-\text{mom}}$ ), and the energy flux ( $F_{\text{energy}}$ ) in the radial direction, and are given by,

$$F_{\text{mass}} = \dot{M}, \quad F_{x-\text{mom}} = (W + \Sigma\vartheta^2), \quad F_{\phi-\text{mom}} = \dot{J} = \dot{M}\lambda + x^2 W_{x\phi} \quad \text{and} \quad F_{\text{energy}} = \dot{M}(\varepsilon - \Phi), \quad (22)$$

where,  $\Phi$  is the gravitational potential. It is quite interesting to see that, the mass flux along the radial direction is  $\dot{M}$ , the momentum flux in the radial direction is the sum of the thermal pressure and the ram pressure, in the azimuthal direction the momentum flux is  $\dot{J}$  or the angular momentum flux, and the energy flux is related to the generalized Bernoulli parameter  $\varepsilon$ . After some straight forward algebra, we find the generalized version of the non-dissipative shock condition in presence of viscosity and cooling, and is given by

$$\dot{M}_+ = \dot{M}_-, \quad (23)$$

$$W_+ + \Sigma_+ \vartheta_+^2 = W_- + \Sigma_- \vartheta_-^2, \quad (24)$$

$$j_+ = j_-, \quad (25)$$

and

$$\varepsilon_+ = \varepsilon_-, \quad (26)$$

where subscripts minus(-) and plus(+) denote the quantities of supersonic and subsonic branches across the shock in a black hole accretion flow, respectively. In the inviscid and adiabatic limit if we put  $\alpha = Q^- = 0$ , we retrieve the original Rankine Hugoniot shock conditions, *i.e.*, equation (25) is redundant and equation (26) reduces to the conservation of the canonical Bernoulli parameter across the shock (Landau & Lifshitz 1959; Chakrabarti 1989). Various authors have used various forms of shock conditions for viscous flow, in the literature. The shocked disc solution with viscosity was obtained by Chakrabarti (1996) and later by (Gu & Lu 2004; Chattopadhyay & Das 2007; Das 2007; Das & Chattopadhyay 2008), by choosing the viscous stress to be proportional to the total pressure, which made equation (25) redundant. Becker *et al.* (2008) on the other hand, used isothermal condition instead of equation (26). In Kumar & Chattopadhyay (2013) and Kumar *et al.* (2014), cooling was ignored, so equation (26) was replaced by the conservation of  $E$  across the shock front. Since, equations (23-26) do not explicitly depend on the form of  $h$ , and viscosity and cooling processes have been considered, therefore this form of shock condition is the most general form of Rankine-Hugoniot type shock conditions obtained by strict conservation of fluxes of the equations of motion by following the prescription laid down by Landau & Lifshitz (1959).

In Kumar & Chattopadhyay (2013), we have discussed various types of dissipative shocks, in which the fraction of thermal energy dissipated was supplied as a parameter. In this paper, we would discuss a special form of dissipative shock by replacing equation (26) with

$$E_+ = E_-. \quad (27)$$

Using equations (23-26), the supersonic branch radial velocity, temperature, and the angular momentum can be obtained from the post-shock quantities and vice versa,

$$\vartheta_-^2 - 2 \left( c_1 - h_- + \frac{\lambda_-^2}{2x_s^2} - \frac{\lambda_- \lambda_0}{x_s^2} + \zeta_- \right) = 0, \lambda_- = \lambda_0 + \frac{c_2 a_-^2}{\Gamma_- \vartheta_-} \text{ and } \Theta_- = \frac{K}{2} (c_0 \vartheta_- - \vartheta_-^2), \quad (28)$$

where  $c_0 = [2\Theta_+/K + \vartheta_+^2]/\vartheta_+$ ,  $c_1 = \vartheta_+^2/2 + h_+ - \lambda_+^2/(2x_s^2) + \lambda_+ \lambda_0/x_s^2 - \zeta_+$ ,  $\zeta_+ = \zeta_{s+} + \zeta_{B+}$ ,  $c_2 = \Gamma_+ \vartheta_+ (\lambda_+ - \lambda_0)/(a_+^2)$  and  $\zeta_- = (f_{\Theta_e}^3 \zeta_{s+} + f_{\Theta_e}^{1/2} \zeta_{B+})/(f_{\vartheta}^2 f_{\Theta}^{1/2})$ . Moreover,  $f_{\Theta_e} = \Theta_{e-}/\Theta_{e+}$ ,  $f_{\vartheta} = \vartheta_-/\vartheta_+$  and  $f_{\Theta} = \Theta_-/\Theta_+$ . All three quantities ( $\vartheta_-$ ,  $\Theta_-$  and  $\lambda_-$ ) in equation 28 are

obtained simultaneously in terms of post-shock quantities which eventually gives us the shock location  $x_s$ .

For dissipative shocks, we use equations (23)-(25) and (27) to relate the post-shock and the pre-shock quantities, and they are

$$\vartheta_-^2 - 2 \left( c_3 - h_- + \frac{\lambda_-^2}{2x_s^2} - \frac{\lambda_- \lambda_0}{x_s^2} \right) = 0, \quad \lambda_- = \lambda_0 + \frac{c_2 a_-^2}{\Gamma_- \vartheta_-} \quad \text{and} \quad \Theta_- = \frac{K}{2} (c_0 \vartheta_- - \vartheta_-^2), \quad (29)$$

where,  $c_3 = \vartheta_+^2/2 + h_+ - \lambda_+^2/(2x_s^2) + \lambda_+ \lambda_0/x_s^2$ .

## 2.2 Solution Procedure

As has been discussed in Section 2.1, the equations of motions, *i.e.*, equations (4)-(6) and (8), can be simplified as gradients of  $\vartheta$  (equation 18),  $\lambda$  (equation 16) and  $\Theta$  (equation 17). Since black hole accretion is necessarily transonic, and the sonic point for dissipative flow is not known a priori, so as the first step to find complete solutions, one need to find a method to compute the location of the sonic point. Moreover, black hole accretion may harbour at least one sonic point, but depending upon boundary conditions the accretion solution may possess two physical sonic points, and one unphysical one. One of the physical sonic point is closer to the horizon and is called inner sonic point ( $x_{ci}$ ), the one further out is called outer sonic point ( $x_{co}$ ) and the unphysical sonic point is situated in between  $x_{ci}$  and  $x_{co}$  and is called the middle sonic point  $x_{cm}$ . The middle sonic point is O type for inviscid, adiabatic flow but is spiral type for dissipative flow. In the domain of a single sonic point, depending on boundary conditions, the single physical sonic point may be located closer to the black hole or may be located far away from the black hole.

### 2.2.1 Method to find the sonic point

In principle, once the flow parameters like  $\varepsilon$ ,  $\lambda_0$ ,  $\alpha$ ,  $\dot{m}$  and  $\beta$  are supplied one should be able to obtain the accretion solution by integrating equations (16)-(18). Since, at least one sonic point exists for black hole accretion, and we do not know the location of the sonic point or the value of  $\lambda_c$  before hand, we have to find sonic point and  $\lambda_c$  by iteration method. Moreover, even though all the flow parameters on the horizon are known, but because of the coordinate singularity on the horizon, we cannot start the integration from the horizon itself. Therefore, we consider the following steps to obtain the sonic points.

*Step 1.* We estimate the asymptotic behaviour of the flow variables at  $x_{in}$  a radial coordinate very close to the horizon, and use it as the starting point of our integration. This method

was successfully employed by Becker & Le (2003) for fixed  $\Gamma$  EoS, here we implement the same method for an EoS described by equation (1). In addition we do not need to make an explicit assumption of free fall close to the horizon. Equation (16) is a first-order differential equation, so we can expand it by Frobenius expansion for  $\lambda(x)$  about  $r_g$  (Becker & Le 2003).

$$\lambda(x) = \lambda_0 + \mathcal{B}(x - r_g)^\delta, \quad x \rightarrow r_g, \quad (30)$$

where constants  $\mathcal{B}$ ,  $\delta$  are to be determined. Combining equations (15 and 16), we obtain

$$\frac{d\lambda}{dx} = 2x\Omega - \frac{\Gamma\vartheta\Omega_K(\lambda - \lambda_0)}{\alpha a^2} \quad (31)$$

Using equation (30) in equation (31), in the limit  $x \rightarrow r_g$  we obtain,

$$\lim_{x \rightarrow r_g} \frac{\Gamma\vartheta\Omega_K}{\alpha a^2} \mathcal{B}(x - r_g)^\delta = \frac{2\lambda_0}{r_g} - \lambda'_0 \quad (32)$$

We replace  $\vartheta$  between equations (32) and (14), use the expression of  $\Omega_K$ , and the definition of  $H$  (equation 7), we obtain,

$$\lim_{x \rightarrow r_g} \frac{\Gamma\dot{\mathcal{M}}K^{1/2}}{\alpha a^2 2\sqrt{2\Theta}x^2(x - r_g)^2(\rho/K)} \mathcal{B}(x - r_g)^\delta = \frac{2\lambda_0}{r_g} - \lambda'_0, \quad (33)$$

where  $\rho/K$  is given by equation (13). A constant value warrants that net exponent of  $(x - r_g)$  goes to zero, *i.e.*,  $\delta = 2$ . Since by equation (30),  $\lambda \rightarrow \lambda_0$  as  $x \rightarrow r_g$ , therefore we have

$$\mathcal{B} = 4\alpha\lambda r_g^2 \frac{\sqrt{2\Theta}}{\Gamma\sqrt{K}\dot{\mathcal{M}}} \exp(k_3)\Theta^{3/2}(3\Theta + 2)^{k_1}(3\Theta + 2/\eta)^{k_2}. \quad (34)$$

We now combine equations (30) and (34), and plug them in equation (11). In addition,  $\vartheta$  in equation (11) is expressed in terms of  $\dot{\mathcal{M}}$ , hence we obtain a polynomial in  $\Theta$ . Now, providing the parameters  $\varepsilon, \lambda_0, \alpha, \xi, \dot{\mathcal{M}}$  and  $\mathcal{F}(x_s) = 1$ , we solve for  $\Theta$  at  $x_{in}$ . Once  $\Theta_{in}$  is obtained,  $a_{in}$ ,  $\vartheta_{in}$  and  $\lambda_{in}$  are easily obtained.

*Step 2.* We now integrate equations (16) — (18) outward from  $x_{in}$ , with the asymptotic flow variables, and simultaneously check the critical point conditions (equations 19- 21).

*Step 3.* Initial solution with an initial guess value of  $\dot{\mathcal{M}}$  will, in all probability, not be a transonic solution. We change the value of  $\dot{\mathcal{M}}$  keeping other flow parameters same, and then again recalculate the asymptotic flow variables at  $x_{in}$ . With the new set of  $\vartheta_{in}$ ,  $\Theta_{in}$ ,  $\lambda_{in}$  we now follow Step 2, until the critical point conditions are satisfied, and obtain the sonic point or critical point ( $x_c$ ) of the flow.

*Step 4.* Once we get value of  $x_c$  and the corresponding  $\lambda_c$ ,  $\vartheta_c$ ,  $\Theta_c$ , we compute  $(d\vartheta/dx)_{x_c}$  and  $(d\Theta/dx)_{x_c}$ .

*Step 5.* Now the integration is continued outwards from  $x_c \rightarrow \infty$  to obtain the global solution.

The global solution might be smooth passing through one  $x_c$ , or may be discontinuous harbouring shocks and therefore passing through both the outer ( $x_{co}$ ) and the inner sonic ( $x_{ci}$ ) points. One set of solution is also possible when the parameter space posses multiple sonic points, but steady state shock conditions are not satisfied.

### 2.2.2 To find the shock:

As the equations of motion are integrated from  $x_c$  outward, we check either for the non-dissipative shock condition (equations 23-26) or the dissipative shock conditions (equations 23-25, 27) we calculate the supersonic branch quantities  $\vartheta_-$ ,  $\Theta_-$ , and  $\lambda_-$  at the tentative jump radius  $\bar{x}_s$ . Using these variables and  $\bar{x}_s$  as the starting point, we solve the equations of motion to find out the outer sonic point of  $x_{co}$  by checking the sonic point conditions (19-21) iteratively. Once  $x_{co}$  is determined, then the corresponding  $\bar{x}_s$  is the tentative shock location. Now supplying  $\bar{x}_s$  in equation (9), we find the Comptonization factor  $\mathcal{F}(\bar{x}_s)$  and update  $Q^-$ . With this new cooling, we recalculate the shock location again by retracing the steps suggested in Sections 2.2.1 and 2.2.2. Once the shock location converges to a value  $x_s$ , we have a self consistent shocked accretion solution.

## 3 RESULTS

The accretion solutions are characterized by the following flow parameters: the generalized Bernoulli parameter  $\varepsilon$ , and  $\dot{m}$  which are constants of motion. Furthermore,  $\lambda_0$  or the angular momentum on the horizon is a constant of integration, and viscosity parameter  $\alpha$  are the two more parameters. On the top of that,  $\xi$  the composition fraction determines the flow composition and therefore the EoS, and  $\beta$  controls the synchrotron emission, by estimating the magnetic energy. It is to be understood that the equations of motion (equations 23-26) are not over determined, because  $\dot{m}$  and  $\beta$  together controls the cooling processes. It is to be remembered that supplying the inner boundary condition ( $\varepsilon$ ,  $\lambda_0$ ,  $\dot{m}$ ) to determine the sonic points in presence of  $\alpha$ ,  $\xi$  and  $\beta$  is equivalent to, supplying the outer boundary condition ( $\varepsilon$ ,  $\lambda_{inj}$ ,  $\dot{m}$ ), where  $\lambda_{inj}$  is the specific angular momentum at the outer boundary. The outer boundary of the disc is symbolized by  $x_{inj}$ . Following eqs. (10), the total surface luminosity of the disc is given by

$$\mathcal{L}_t = 4\pi \int \mathcal{F}(x_s)(Q_S^- + Q_B^-)\Sigma x dx, \quad \text{and } \ell = \mathcal{L}_t/L_{\text{Edd}}, \quad (35)$$

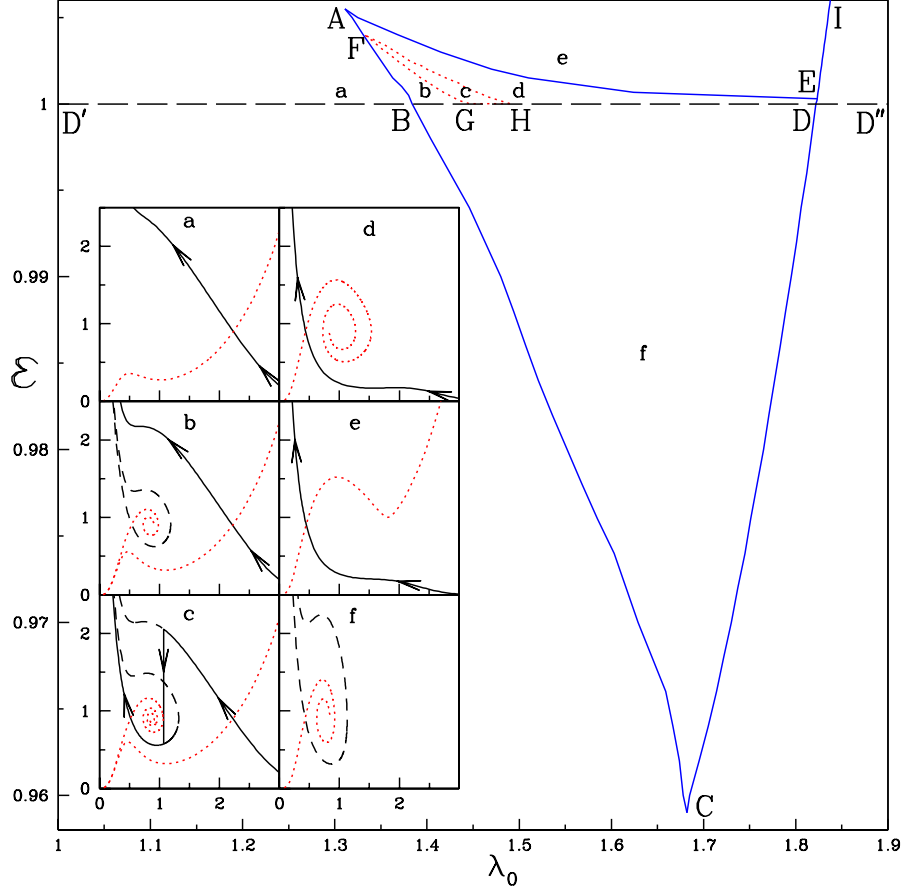


**Figure 1.** Division of the parameter space in  $\varepsilon - \lambda_0$  according to number of critical points and representative accretion solutions. Area ABDEA and BCDB has three and two critical points, respectively. Area outside the bounded region D'BAEI and  $\varepsilon > 1$  has single critical point, but for regions outside D'BCDEI and  $\varepsilon < 1$  no critical points exist. Inset panels labelled as a, b, c, d, e, and f present Mach number  $M = v/a$  versus  $\log(x)$ , corresponding to the  $\varepsilon$ ,  $\lambda_0$  values at the locations marked in the parameter space. The dotted region FGHF is the shock parameter space, and in panel (c) the vertical jump shows the position of the shock. Accretion solutions are represented by solid (online black) curve. This parameter space and the associated solutions are for  $\alpha = 0.05$ ,  $\beta = 0.01$  and  $\dot{m} = 0.1$ .

where  $\mathcal{L}_t$  is the total luminosity and  $\ell$  is the dimensionless luminosity in units of  $L_{\text{Edd}} \approx 1.3 \times 10^{38} (M/M_\odot)$ . The relation between Eddington accretion rate and Eddington limit is  $\dot{M}_{\text{Edd}} = L_{\text{Edd}}/c^2$ .

### 3.1 All possible transonic accretion solutions for $e^- - p^+$ flow

In Fig. 1, we present the full  $\varepsilon - \lambda_0$  parameter space, and all possible accretion solutions, corresponding to  $\xi = 1.0$  or  $e^- - p^+$  flow,  $\alpha = 0.05$ ,  $\beta = 0.01$  and  $\dot{m} = 0.1$ . The solutions or the Mach number distributions  $M (= v/a)$  for various parameters are plotted in the inset. In Fig. 1, the inset panel labelled ‘a’ presents  $M$  versus  $\log(x)$ , corresponding to location ‘a’ in the energy-angular momentum parameter space for coordinates  $(\varepsilon, \lambda_0 = 1.0005, 1.3)$ . Increasing  $\lambda_0$ , we move to locations ‘b’ ( $\varepsilon, \lambda_0 = 1.0005, 1.41$ ), ‘c’ ( $\varepsilon, \lambda_0 = 1.0005, 1.425$ ) and ‘d’ ( $\varepsilon, \lambda_0 = 1.0005, 1.52$ ). And then for higher  $\varepsilon$ , solution of panel ‘e’ represents solution

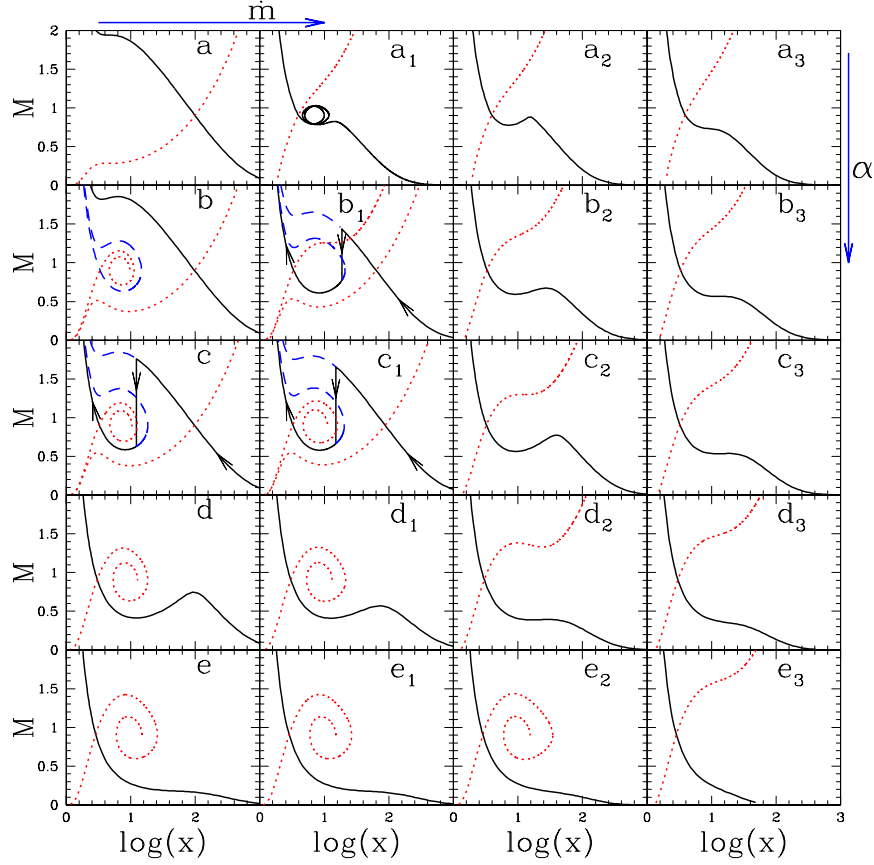


**Figure 2.** Effect of accretion rate and the viscosity parameter on shock-free inviscid flow. The Mach number  $M$  are plotted with  $\log(x)$  in all the panels, for parameters  $\varepsilon = 1.001$ ,  $\lambda_0 = 1.46$ ,  $\beta = 0.1$  and  $\xi = 1.0$ . (a) Shock free solution with only  $x_{co}$  in the inviscid limit. Vertically down  $\downarrow$  viscosity increases *e.g.*, (a - e),  $\alpha = 0.0, 0.025, 0.03, 0.048$  and  $0.065$ , respectively, and  $\chi = 0.0$ . Left to right,  $\dot{m}$  increases. For panels  $a_1 - a_3$ , we have cooling *i.e.*,  $\chi = 1.0$  and the accretion rates are  $\dot{m} = 3.5, 4.0$  and  $5.0$ . For panels  $b_1 - b_3$ ,  $\chi = 1.0$  and  $\dot{m} = 0.7, 1.4$  and  $2.1$ . For panels  $c_1 - c_3$ ,  $\chi = 1.0$  and  $\dot{m} = 0.2, 0.8$  and  $1.6$ . For panels  $d_1 - d_3$ ,  $\chi = 1.0$  and  $\dot{m} = 0.1, 0.5$  and  $1.0$ . For panels  $e_1 - e_3$ ,  $\chi = 1.0$  and  $\dot{m} = 0.01, 0.1$  and  $1.0$ . Wind type solutions are plotted as dotted curve (red online) and dashed (blue) part of the transonic solution which is not followed by the flow.

corresponding to location ‘e’ ( $\varepsilon, \lambda_0 = 1.003, 1.55$ ), and panel ‘f’ corresponds to solution for ( $\varepsilon, \lambda_0 = 0.985, 1.6$ ). The global transonic accretion solutions in the inset are represented by solid curve (online black), and solutions which represent wind-type solutions are represented by the dotted curve (online red). The dashed curve represents the transonic solution through which matter may pass. Accretion flows with any value of  $\varepsilon$  and  $\lambda_0$  in the bounded region ABDEA has three sonic points, and have a combination of closed and global solutions (*e.g.*, Figs. 1b — e). In the domain of multiple sonic points, if the steady shock solution cannot be obtained, and in addition, the solution through  $x_{co}$  do not connect the horizon and infinity, then the solutions through  $x_{co}$  cannot be determined exactly, and so, only solutions through inner sonic point are shown for Fig. 1d. The rough location of  $x_{co}$  can be ascertained for Fig. 1d, at the location where global solution through  $x_{ci}$  (solid and online black), shows a maximum. An ADAF-type solution, *i.e.*, monotonic  $M$  distribution



through  $r_{\text{ci}}$ , is shown in Fig. 1e. On the other hand, flows with  $\varepsilon$  and  $\lambda_0$  in the region BCDB have two critical points, and produces only closed topologies and therefore no global transonic solution (Fig. 1f). Within ABDEA, the bounded region FGHF produces steady, non-dissipative shocked solutions (*e.g.*, Fig. 1c), which are obtained from equations (23)-(26). The region outside BAEI and  $\varepsilon \geq 1$ , there is only one sonic point (*e.g.*, Figs. 1a & f). Fig. 1a, has low angular momentum and therefore produces a Bondi-type solution characterized by a single sonic point far away from the horizon, even in presence of dissipation. Fig. 1e, on the other hand produces a solution which is mostly subsonic and becomes transonic close to the horizon, and is similar to ADAF-type solutions. Regions outside D'BCD and  $\varepsilon < 1$  and right of the curve DI, there exists no critical point, and consequently steady state black hole accretion is not allowed for such inner boundary conditions. The coordinates of the important points which represents the multiple sonic point domain in the energy-angular momentum parameter space are A (1.0055, 1.311), B (1.0, 1.385), C (0.959, 1.682), D (1.0, 1.822) and E (1.0003, 1.824).

Having shown how solution of electron-proton flow depends on  $\varepsilon$  and  $\lambda_0$  for given values of  $\alpha$ ,  $\beta$  and  $\dot{m}$ , we now present dependence of advective solutions on  $\alpha$  and  $\dot{m}$  for given values of  $\varepsilon$  and  $\lambda_0$ . We choose flow parameters  $(\varepsilon, \lambda_0) = (1.001, 1.46)$  which produces shock-free solution with a single  $x_{\text{co}}$ -type sonic point in the inviscid limit, *i.e.*, for  $\alpha = \chi = 0$  (Fig. 2a). Panels on the left, Figs. 2(a)—(e), represent solutions without cooling *i.e.*,  $\chi = 0.0$ , but increasing viscosity  $\alpha = 0.025$  (Fig. 2b),  $\alpha = 0.03$  (Fig. 2c),  $\alpha = 0.048$  (Fig. 2d),  $\alpha = 0.065$  (Fig. 2e). We show that a shock-free solution through a single  $x_{\text{co}}$  in the inviscid limit (Fig. 2a), enters multi-critical point domain (Fig. 2b), and eventually generates shock (Fig. 2c) as  $\alpha$  is increased for the same inner boundary condition *i.e.*,  $\varepsilon - \lambda_0$ . Further increase of  $\alpha$  removes steady shock while still being in the multi-critical point domain (Fig. 2d), and eventually produces a monotonic shock-free solution through  $x_{\text{ci}}$  or ADAF type solution. In Figs. 2(a)-(a<sub>3</sub>), the solutions are inviscid, but  $\dot{m}$  is increased step by step to values 3.5 (Fig. 2a<sub>1</sub>), 4.0 (Fig. 2a<sub>2</sub>), and 5.0 (Fig. 2a<sub>3</sub>). For Figs. 2 (b<sub>1</sub>)-(b<sub>3</sub>),  $\alpha = 0.025$  (same as Fig. 2b),  $\dot{m}$  varies from 0.7, 1.4 and 2.1, respectively. For Figs. 2(c<sub>1</sub>)-(c<sub>3</sub>),  $\alpha$  is same as Fig. 2c, but  $\dot{m}$  varies from 0.2, 0.8 and 1.6, respectively. The accretion rate  $\dot{m}$  increases from 0.1 in Fig. 2d<sub>1</sub>, to 0.5 in Fig. 2d<sub>2</sub> and then up to 1.0 in Fig. 2d<sub>3</sub>, and has the same  $\alpha$  as Fig. 2d. On the other hand,  $\alpha$  of Fig. 2e is used for Figs. 2(e<sub>1</sub>)-(2e<sub>3</sub>), but accretion rates are  $\dot{m} = 0.01$  (Fig. 2e<sub>1</sub>),  $\dot{m} = 0.1$  (Fig. 2e<sub>2</sub>) and  $\dot{m} = 1.0$  (Fig. 2e<sub>3</sub>). Therefore, it is clear that the very inner boundary condition (read  $\varepsilon - \lambda_0$ ) which produces a shock-free, monotonic solution with only

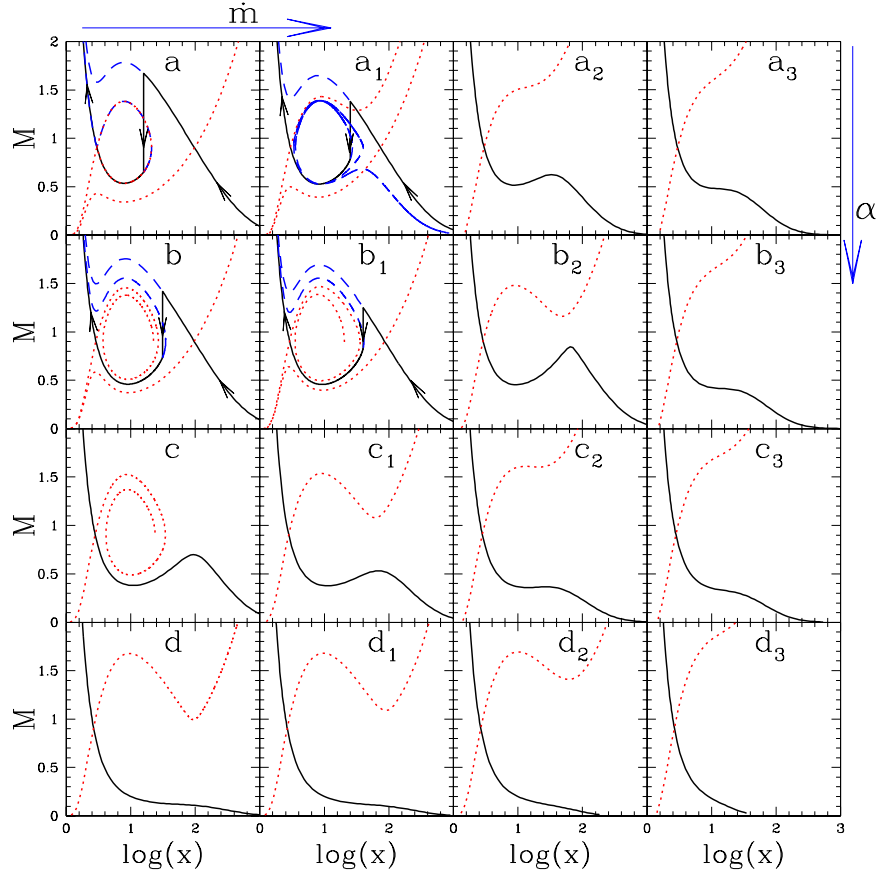


**Figure 3.** Effect of accretion rate and viscosity parameter for boundary conditions which support steady shock in inviscid flow.  $\varepsilon = 1.001$ ,  $\lambda_0 = 1.55$ ,  $\beta = 0.1$  and  $\xi = 1.0$  are same for all solutions. (a) to (d)  $\chi = 0.0$  and  $\alpha = 0.0, 0.01, 0.02$  and  $0.043$ , respectively. (a<sub>1</sub>) to (a<sub>3</sub>)  $\chi = 1.0$  and  $\dot{m} = 0.2, 0.8, 1.4$  (b<sub>1</sub>) to (b<sub>3</sub>)  $\chi = 1.0$  and  $\dot{m} = 0.03, 0.18, 0.9$ . (c<sub>1</sub>) to (c<sub>3</sub>)  $\chi = 1.0$  and  $\dot{m} = 0.1, 0.5, 1.0$ . (d<sub>1</sub>) to (d<sub>3</sub>)  $\chi = 1.0$  and  $\dot{m} = 0.01, 0.1, 1.0$ . Wind-type solutions are plotted as dotted curve (red online), and dashed (blue) part of the transonic solution which is not followed by the flow in presence of shock.

one  $x_{co}$  sonic point in the inviscid limit, for different  $\alpha$  and  $\dot{m}$  will produce such varied  $\lambda$  and  $\Theta$  distributions that would generate solutions comprising multiple-sonic points, shocks, or monotonic ADAF-type solutions. In the next figure we consider a different inner boundary condition. In Fig. 3a, we consider the parameters ( $\varepsilon, \lambda_0 = 1.001, 1.55$ ), which in the inviscid limit produces shock at  $x_s = 15.936$ . The composition of the flow is  $\xi = 1.0$ . We increase  $\alpha$  as we go vertically down, which are  $\alpha = 0.01$  (Fig. 3b),  $\alpha = 0.02$  (Fig. 3c) and  $\alpha = 0.043$  (Fig. 3d), but keep  $\chi = 0$ . We turn on  $\chi$ , and increase  $\dot{m}$  to the right, while keeping  $\alpha$  in each row the same. In Figs. 3a<sub>1</sub>  $\rightarrow$  3a<sub>3</sub>,  $\alpha = 0, \beta = 0.1, \chi = 1$ , but  $\dot{m} = 0.2, 0.8, 1.4$ , respectively. In Figs. 3 (b<sub>1</sub>) to (b<sub>3</sub>),  $\alpha = 0.01, \chi = 1$ , but  $\dot{m} = 0.03, 0.18, 0.9$ , respectively. For Figs. 3 (c<sub>1</sub>) to (c<sub>3</sub>) the parameters are  $\alpha = 0.02, \chi = 1$  and  $\dot{m} = 0.1, 0.5, 1.0$ , respectively. Shocked solutions seems to be maintained for a range of  $\alpha$  and  $\dot{m}$ , but playing with various flow parameters generates all possible solutions, including ADAF type solutions. Figs. 3 (a)-(d<sub>3</sub>)

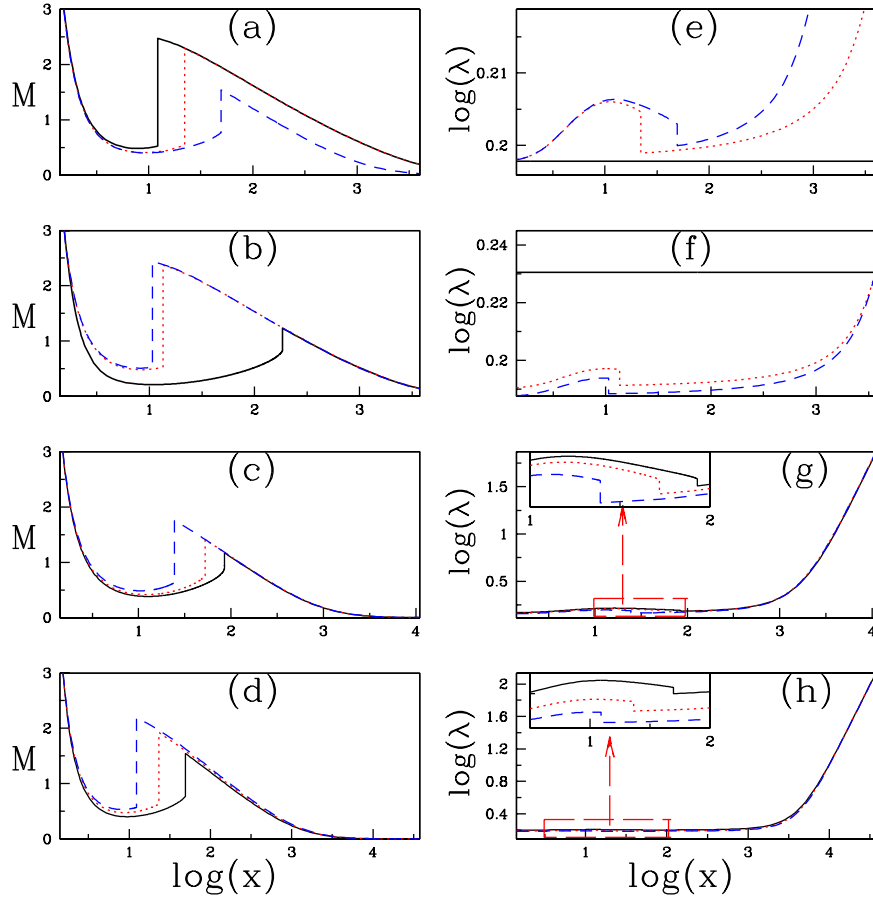


**Figure 4.** Variation of  $M$  (a-d) and corresponding  $\log(\lambda)$  (e-h) with  $\log(x)$ , for  $e^- - p^+$  flow. Solutions (a and e) are plotted for same  $\varepsilon = 1.0001$ ,  $\lambda_0 = 1.577$ . Each curve corresponds to  $\alpha = 0.0$ ,  $\chi = 0.0$  and a shock at  $x_s = 12.2236$  (solid, online black),  $\alpha = 0.01$ ,  $\chi = 0.0$  and a shock at  $x_s = 22.1412$  (dotted, online red) and  $\alpha = 0.01$ ,  $\chi = 1.0$  and a shock at  $x_s = 49.4872$  (dashed, online blue). Each curve in (b and f) is generated for  $\alpha = 0.0$ ,  $\chi = 0.0$  with  $x_s = 183.9687$  (solid, online black),  $\alpha = 0.01$ ,  $\chi = 0.0$  with  $x_s = 13.5259$  (dotted, online red) and  $\alpha = 0.01$ ,  $\chi = 1.0$  with  $x_s = 10.6728$  (dashed online blue), but for same outer boundary conditions  $\lambda_{\text{inj}} = 1.7$ ,  $\Theta_{\text{inj}} = 9.811 \times 10^{-2}$  and  $\vartheta_{\text{inj}} = 1.928 \times 10^{-3}$ , at  $x_{\text{inj}} = 3686.02$ . Plots a and e, b and f have common parameters,  $\beta = 0.1$  and  $\dot{m} = 0.1$ . Each curve in (c and g) is plotted with  $\alpha = 0.0494$  and produces a shock at  $x_s = 85.1545$  (solid, online black),  $\alpha = 0.0534$  and  $x_s = 52.3582$  (dotted, online red),  $\alpha = 0.0545$  and  $x_s = 24.5147$  (dashed, online blue) and  $\chi = 1.0$  but keeping other parameters,  $\lambda_{\text{inj}} = \lambda_K(x_{\text{inj}}) = 74.12$ ,  $\Theta_{\text{inj}} = 0.3999$  and  $\vartheta_{\text{inj}} = 4.3568 \times 10^{-5}$  fixed at the outer boundary  $x_{\text{inj}} = 10986.38$  with  $\beta = 0.01$ ,  $\dot{m} = 0.1$ . Each curve in (d and h) are plotted with different accretion rates  $\dot{m} = 0.1$  (solid, online black),  $0.3$  (dotted, online red) and  $0.5$  (dashed, online blue) and  $\alpha = 0.01$ ,  $\beta = 0.1$  are fixed. We keep  $\lambda_{\text{inj}} = \lambda_K(x_{\text{inj}}) = 136.67$ ,  $\Theta_{\text{inj}} = 3.554$  and  $\vartheta_{\text{inj}} = 1.1571 \times 10^{-5}$  are fixed at the outer boundary  $x_{\text{inj}} = 37354.32$ . The shocks are at  $x_s = 49.4872$ ,  $23.13107$  and  $12.3237$ , respectively.

show that the closed topology through  $x_{\text{ci}}$  in the inviscid limit, opens up with the increase of viscosity and cooling.

In Figs. 4 (a)-(h), we compare accretion solutions by varying  $\alpha$ ,  $\chi$  or  $\dot{m}$  but for either same inner boundary condition or same outer boundary condition. In Figs. 4 (a)-(d) we plot  $M$ , and in Figs. 4 (e)-(h) we plot  $\log(\lambda)$  with  $\log(x)$ . Each pair of horizontal panels show the Mach number and angular momentum distribution of flows with same boundary condition. For example, Figs. 4 (a) and (e) presents  $M$  and  $\log(\lambda)$  distribution of accretion flows with same inner boundary condition, *i.e.*,  $\varepsilon = 1.0001$ , and  $\lambda_0 = 1.577$ , where each curve represents  $\alpha = 0.0$ ,  $\chi = 0.0$  (solid, online black),  $\alpha = 0.01$ ,  $\chi = 0.0$  (dotted,

online red) and  $\alpha = 0.01$ ,  $\chi = 1.0$  (dashed, online blue). Clearly,  $\lambda = \lambda_0$  is a constant of motion for inviscid and adiabatic solution. Evidently, the shock recedes as viscosity is turned on ( $x_s = 12.2236 \rightarrow 22.1412$ ), and then further recedes to  $x_s = 49.4872$  as the cooling is turned on over and above the viscous dissipation. Since the effect of viscosity is to reduce angular momentum inwards, and the effect of cooling is to reduce temperature inwards, therefore, keeping same inner boundary and increasing viscosity and cooling implies both angular momentum and temperature increases outwards. Higher temperature and angular momentum means the shock front is shifted outwards. In Figs. 4 (b) and (f), we again compare inviscid flow (solid, online black), with flow in presence of viscosity, *i.e.*,  $\alpha = 0.01$ , and  $\chi = 0.0$  (dotted, online red), and viscous flow in presence of cooling, *i.e.*,  $\alpha = 0.01$ ,  $\chi = 1.0$  (dashed, online blue), but now the flows are launched with the same outer boundary condition, *i.e.*,  $\lambda_{\text{inj}} = 1.7$ ,  $\Theta_{\text{inj}} = 9.811 \times 10^{-2}$  and  $\vartheta_{\text{inj}} = 1.928 \times 10^{-3}$ , at the injection radius  $x_{\text{inj}} = 3686.02$ . The accretion rate is  $\dot{m} = 0.1$  and  $\beta = 0.1$  for the flow with  $\chi = 1$ . Since in this case we start with the same temperature, angular momentum and velocity at the outer boundary, viscosity and cooling processes decrease both  $\lambda$  and  $\Theta$  inwards. Therefore, for flows starting with same outer boundary condition, the net effect of increasing viscosity and cooling is to reduce both the centrifugal force and the pressure, so the shock front shifts closer to the horizon for viscous fluid with and without cooling, compared to the inviscid flow. In Figs. 4c & 4g, we compare viscous flows in presence of cooling ( $\beta = 0.01$ ,  $\dot{m} = 0.1$  and  $\chi = 1.$ ), and starting with the same outer boundary condition ( $\lambda_{\text{inj}} = \lambda_K(x_{\text{inj}}) = 74.12$ ,  $\Theta_{\text{inj}} = 0.3999$  and  $\vartheta_{\text{inj}} = 4.3568 \times 10^{-5}$  at  $x_{\text{inj}} = 10986.38$ ), but now for different viscosity parameters, namely,  $\alpha = 0.0494$  (solid online black),  $0.0534$  (dotted, online red),  $0.0545$  (dashed, online blue). In the previous panel, the solution started with sub-Keplerian flow at the outer boundary. In this figure we compare flows with different  $\alpha$ , but in presence of same cooling parameters, and starting with Keplerian angular momentum (indicated by suffix K) at the outer boundary. Increase of  $\alpha$  shows that the reduction of  $\lambda$  causes the shock to shift inward (see inset), even in presence of cooling. This shows that  $x_s$  reduces with increasing  $\alpha$  for flows starting with same outer boundary condition. In the next pair of panels Figs. 4 (d) and (h), we compare accretion solutions starting with the same outer boundary condition ( $\lambda_{\text{inj}} = \lambda_K(x_{\text{inj}}) = 136.67$ ,  $\Theta_{\text{inj}} = 3.554$  and  $\vartheta_{\text{inj}} = 1.1571 \times 10^{-5}$  at  $x_{\text{inj}} = 37354.32$ ), and same  $\alpha = 0.01$ , but different  $\dot{m} = 0.1$  (solid, online black),  $\dot{m} = 0.3$  (dotted, online red) and  $\dot{m} = 0.5$  (dashed, online blue), in other words, we study the effect of cooling in a viscous flow starting with the same outer boundary condition. In this case, although cooling do not

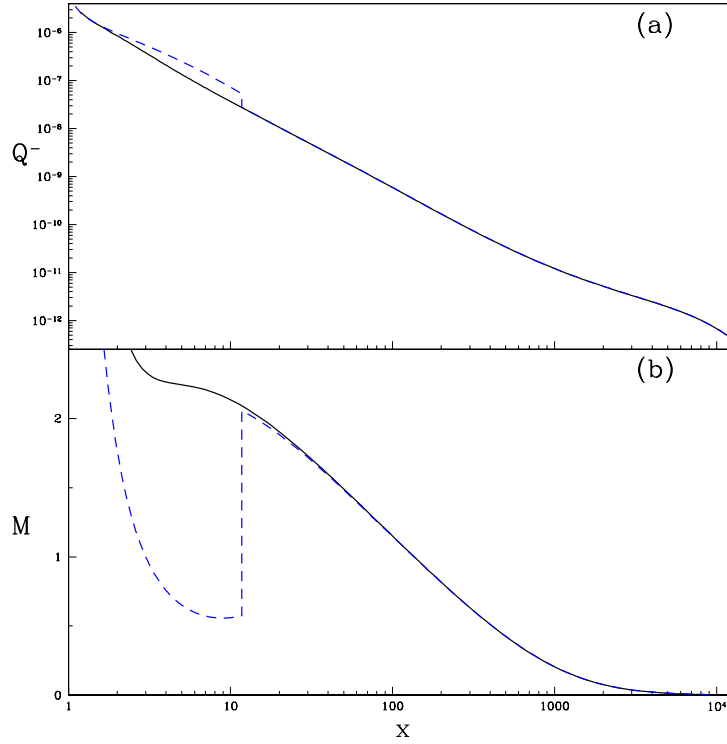


**Figure 5.** Variation of emissivity per unit mass  $Q^-$  (a) and  $M$  (b) with  $x$ . Each curve represents a shock free (solid, online black) and shocked accretion solution (dashed, online blue) generated with the same  $\lambda_{\text{inj}} = \lambda_K(x_{\text{inj}}) = 82.51$  at  $x_{\text{inj}} = 13614.44$ ,  $\varepsilon = 1.0005$ ,  $\beta = 0.01$  and  $\dot{m} = 0.1$ . The shocked solution is generated with  $\alpha = 0.05$  and the shock free for  $\alpha = 0.0505$ . Both the solutions are for  $e^- - p^+$  flow. Luminosities for shock free and shocked solutions are  $\ell = 1.40 \times 10^{-4}$  and  $1.67 \times 10^{-4}$ , respectively.

directly affect the angular momentum equation (16), but it affects the entropy equation and therefore the thermal energy, which reduces the post-shock pressure. As a result shock moves inwards with the increase of cooling. Since kinematic viscosity parameter (*i.e.*,  $\nu$ , defined in equation 5) depends on both  $\alpha$  and  $a^2$ , so cooling processes will affect  $a$  and thereby in an indirect way cooling processes will affect the angular distribution too, as is shown in Fig. 4h.

We compare the emissivity per unit mass *i.e.*,  $Q^-$  (Fig. 5a) and the Mach number  $M$  (Fig. 5b) between a shock free (solid, online black) and a shocked (dashed, online blue) accretion solution, starting with the same outer boundary condition  $\varepsilon = 1.0005$ ,  $\beta = 0.01$  and  $\dot{m} = 0.1$  and  $\lambda_{\text{inj}} = \lambda_K(x_{\text{inj}}) = 82.51$  at  $x_{\text{inj}} = 13614.44$ . The shocked solution is generated with  $\alpha = 0.05$  and the shock-free for  $\alpha = 0.0505$ . Although the radiative output is almost similar in the outer regions, but the post shock flow is more luminous. The over all luminosity of shocked solution is more compared to the shock free solution, even for flow with same composition, outer boundary condition and  $\dot{m}$ . Although we can choose to compare even

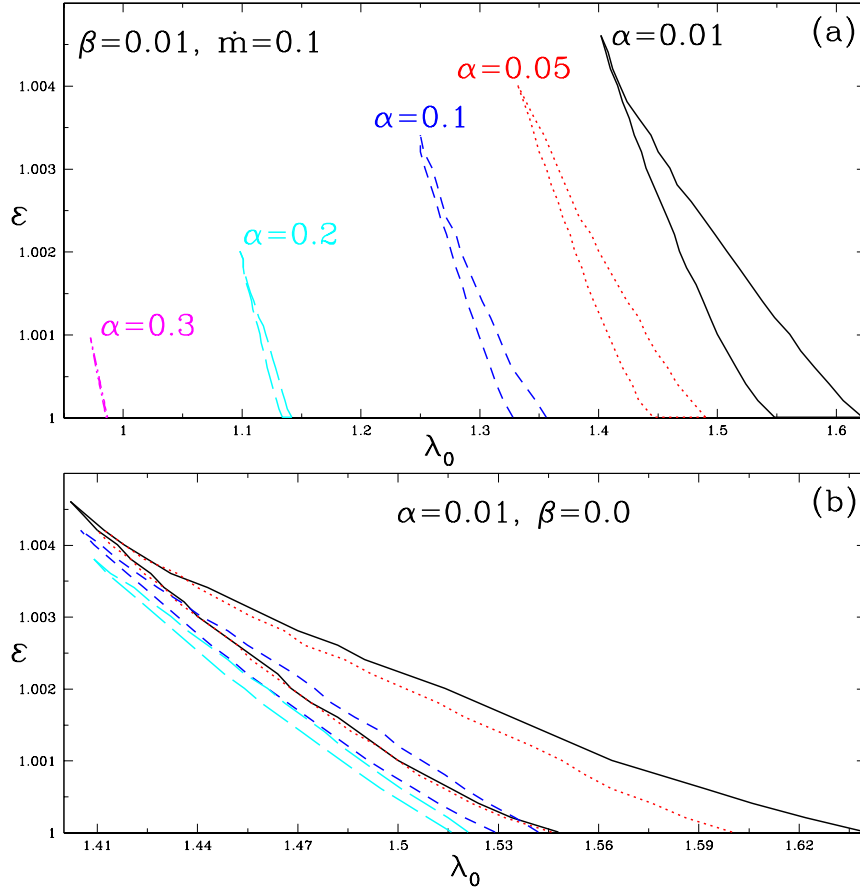


**Figure 6.** (a) Non-dissipative shock parameter space with general Bernoulli parameter ( $\varepsilon$ ) versus specific angular momentum ( $\lambda_0$ ) for  $\alpha = 0.01$  (solid, online black),  $0.05$  (dotted, online red),  $0.1$  (dashed, online blue),  $0.2$  (long-dashed, online cyan) and  $0.3$  (dotted-dashed, online magenta) and with constant cooling parameters,  $\dot{m} = 0.1$  and  $\beta = 0.01$ . (b)  $\varepsilon$ - $\lambda_0$  parameter space for non-dissipative shock for different  $\dot{m} = 0.1$  (solid, online black),  $1.0$  (dotted, online red),  $10.0$  (dashed, online blue) and  $20.0$  (long-dashed, online cyan) and keeping  $\alpha = 0.01$  and  $\beta = 0.0$  fixed. Both the plots are for  $e^- - p^+$  flow.

hotter shock free and shocked solutions, but the greater Comptonization efficiency of shocked solution will in general be more luminous and will also produce a harder spectrum.

In Fig. 6a, we plot the non-dissipative shock parameter space  $\varepsilon - \lambda_0$  of accretion flow in presence of cooling ( $\chi = 1$ ,  $\beta = 0.01$ , and  $\dot{m} = 0.1$ ), but for different viscosity parameters  $\alpha = 0.01$  (solid, online black),  $0.05$  (dotted, online red),  $0.1$  (dashed, online blue),  $0.2$  (long-dashed, online cyan), and  $0.3$  (dotted-dashed, online magenta). One can obtain steady shocks at  $\alpha > 0.3$  in presence of cooling too. In Fig. 6b, we plot shock parameter space  $\varepsilon - \lambda_0$  of accretion flow for a particular  $\alpha = 0.01$  but for different accretion rate  $\dot{m} = 0.1$  (solid, online black),  $1.0$  (dotted, online red),  $10.0$  (dashed, online blue) and  $20.0$  (long-dashed, online cyan), however, with synchrotron processes ignored, *i.e.*,  $\beta = 0$ . It is interesting to note that shocked accretion solution can be obtained for fairly high  $\alpha$  and  $\dot{m}$ .

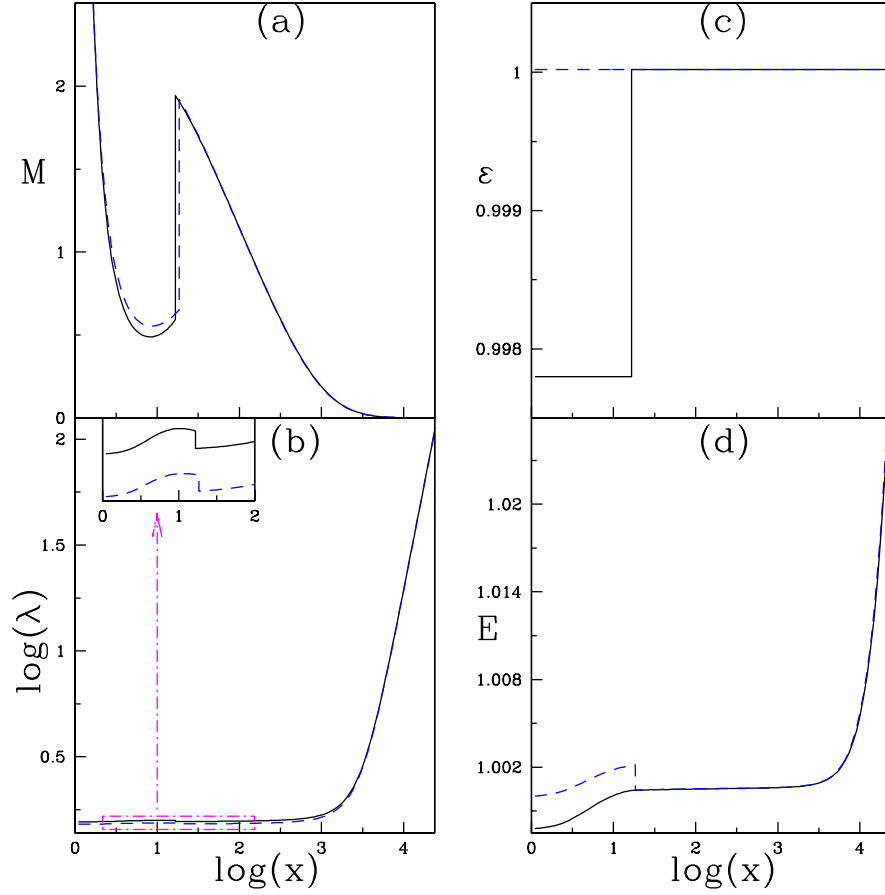


**Figure 7.** Variation of various physical quantities of the accretion flow such as Mach number  $M$  in plot (a), specific angular momentum  $\lambda$  in plot (b), general Bernoulli parameter  $\varepsilon$  in plot (c), and grand specific energy  $E$  in plot (d) are plotted with radial distance  $\log(x)$ . In all plots solid (online black) curves represent dissipative shock and dashed (online blue) curves represent non-dissipative shock solutions and having shock locations at 16.61 and 18.51, respectively. The solutions are generated for  $\alpha = 0.01$ ,  $\beta = 0.01$ , and  $\dot{m} = 1$ . Outer boundary condition is  $\varepsilon = 1.000021$ ,  $\lambda_{\text{inj}} = \lambda_K(x_{\text{inj}}) = 109.19$  at  $x_{\text{inj}} = 23842.73$ . For dissipative shock, the energy dissipated at the shock is  $\Delta\varepsilon = 0.00221$ .

### 3.1.1 Dissipative shock in accretion flow

All shocked solutions presented in the preceding subsection have been examples of non-dissipative shocks obtained by solving equation (28). However, in section 2.1.2, we have discussed if the energy flux is not conserved and still there is a shock, then that would be considered as a dissipative shock. The conditions for a dissipative shock is presented by equation (29). In Figs. 7a-7d, we compare accretion solutions starting with the same outer boundary condition [ $\varepsilon = 1.000021$ ,  $\lambda_{\text{inj}} = \lambda_K(x_{\text{inj}}) = 109.19$  at  $x_{\text{inj}} = 23842.73$ ], same  $\alpha = 0.01$ ,  $\beta = 0.01$  and  $\dot{m} = 1$ , but one solution harbours dissipative shock (solid online black) and the other solution harbours non-dissipative shock (dashed online blue). We compare  $M$  (Fig. 7a),  $\log(\lambda)$  (Fig. 7b),  $\varepsilon$  (Fig. 7c) and  $E$  (Fig. 7d) as a function of  $\log(x)$ . Conservation of  $E$  across the shock is equivalent to a discontinuous decrement in  $\varepsilon$  across the shock (solid curve in Fig. 7c), corresponding to an energy dissipation of  $\Delta\varepsilon = 0.00221$ .

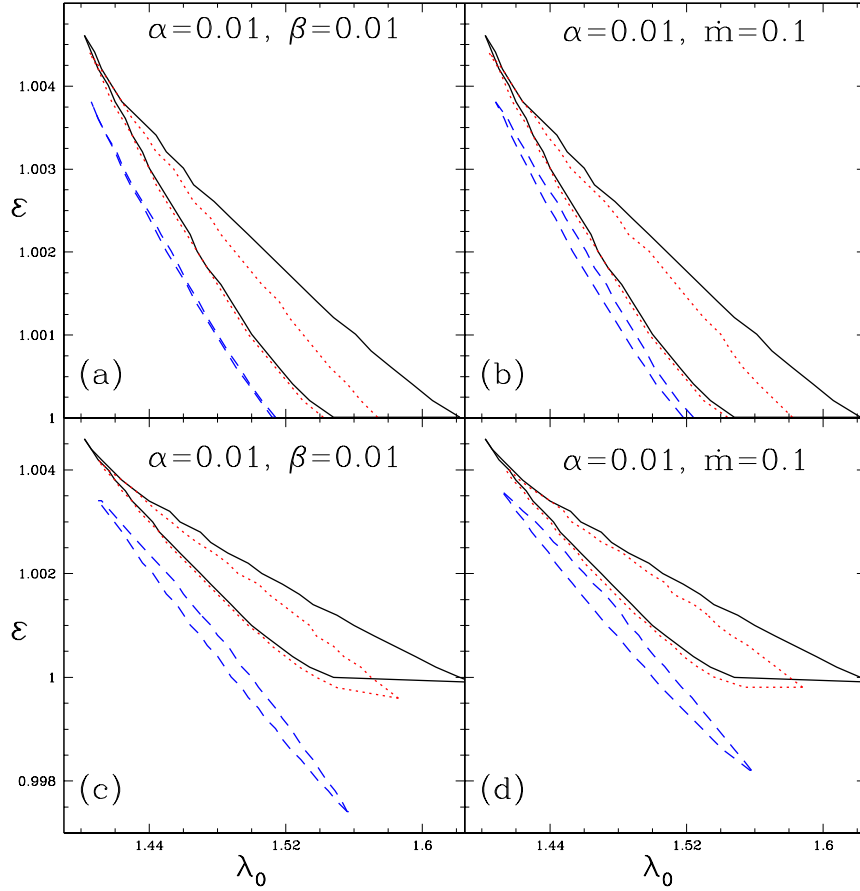


**Figure 8.**  $\varepsilon - \lambda_0$  parameter space for non-dissipative (a and b) and dissipative (c and d) shocks in the flow. Bounded regions in (a, c) are plotted with different accretion rates,  $\dot{m} = 0.1$  (solid line), 1.0 (dotted line) and 10.0 (dashed line) but keeping  $\beta = 0.01$  fixed, and regions in (b, d) are plotted with different  $\beta = 0.01$  (solid line), 0.1 (dotted line) and 1.0 (dashed line) but keeping  $\dot{m} = 0.1$  fixed. All plots are for the same viscosity parameter,  $\alpha = 0.01$ .

Compared to the non-dissipative shock, the dissipative shock forms closer to the horizon because of  $\Delta\varepsilon$  released at the dissipative shock. It is also clear from Figs. 7c and 7d, that  $\varepsilon$  is a constant of motion in presence of viscous dissipation and cooling processes, and  $E$  is not. In Figs. 8a-8d, we plot the  $\varepsilon - \lambda_0$  shock parameter space for non-dissipative shock (Figs. 8a and 8b) and dissipative shocks (Figs. 8c & 8d). In Figs. 8a and 8c, the steady shock parameter space are bounded regions for  $\dot{m} = 0.1$  (solid, online black),  $\dot{m} = 1$  (dotted, online red), and  $\dot{m} = 10$  (dashed, online blue), all the plots are generated for given values of  $\alpha = 0.01$  and  $\beta = 0.01$ . In Figs. 8b and 8d, the shock parameter space are the bounded regions characterized by  $\beta = 0.01$  (solid line), 0.1 (dotted line) and 1.0 (dashed line) but keeping  $\alpha = 0.01$ , and  $\dot{m} = 0.1$  fixed. So in Figs. 8a and 8c, we compare non-dissipative and dissipative shocks for same proportion of synchrotron losses but different mass supply, and in Figs 8b and 8d, we compare non-dissipative and dissipative shocks for same mass supply but different synchrotron losses. We kept the viscosity parameter same to see the effect of



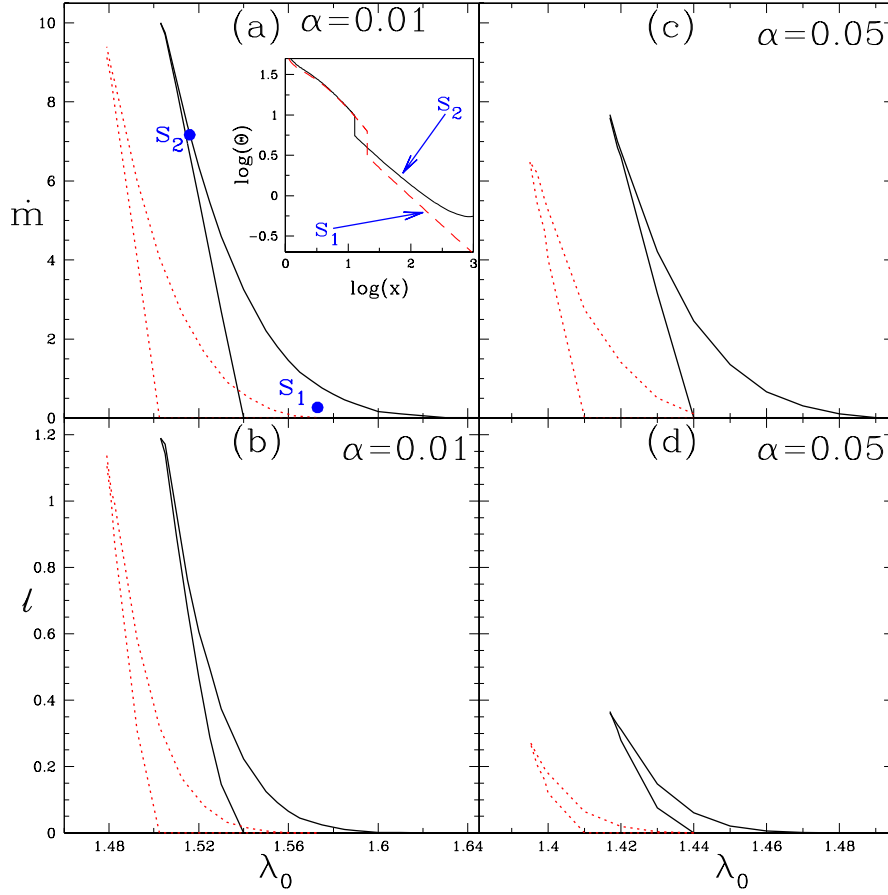


**Figure 9.** Shock parameter space  $\dot{m} - \lambda_0$  in panels (a and c) and corresponding luminosities  $\ell$  in panels (b and d). Plots (a and b) are generated for viscosity parameter,  $\alpha = 0.01$  and plots (c and d) are generated for  $\alpha = 0.05$ . Each curve corresponds to,  $\varepsilon = 1.0001$  (solid line) and  $1.001$  (dotted line). We keep  $\beta = 0.01$  same for all the plots. Inset in (a),  $\Theta$  as a function of  $x$  in log-log scale. Solution  $S_1$  (shown in  $\dot{m} - \lambda_0$  space)  $\varepsilon = 1.0001$ ,  $\lambda_0 = 1.57$ ,  $\alpha = 0.01$ ,  $\beta = 0.01$ ,  $\dot{m} = 0.1$ ,  $x_s = 20.02547$  and disc luminosity  $\ell = 2.766 \times 10^{-4}$ . Solution  $S_2$  (shown in  $\dot{m} - \lambda_0$  space) is for  $\varepsilon = 1.0001$ ,  $\lambda_0 = 1.515$ ,  $\alpha = 0.01$ ,  $\beta = 0.01$ ,  $\dot{m} = 7.0$ ,  $x_s = 12.73524$  and disc luminosity  $\ell = 0.677$ . All the plots are for  $e^- - p^+$  flow.

$\dot{m}$  and  $\beta$ . Clearly the parameter ranges for dissipative steady shock is larger. Evidently, the combined parameter space for both non-dissipative and dissipative shocks is quite significant. From Figs. 6a-6b and 8a-8d, it is clear that steady shock may exist for fairly extreme flow parameters like super Eddington accretions rates,  $\alpha \gtrsim 0.3$ , and fairly high magnetic energy.

### 3.1.2 Hyper-accretion rate

In Figs. 9a and 9c, we plot shock parameter spaces *i.e.*, bounded region of  $\dot{m} - \lambda_0$  and the corresponding  $\ell - \lambda_0$  for a viscosity parameter  $\alpha = 0.01$ , and in Figs. 9b and 9d, the  $\dot{m} - \lambda_0$  and  $\ell - \lambda_0$  shock parameter spaces for  $\alpha = 0.05$ . Each curve are plotted for  $\varepsilon = 1.0001$  (solid, online black) and  $\varepsilon = 1.001$  (dotted, online red). For all the plots  $\chi = 1$  and  $\beta = 0.01$ . It is interesting to note that a steady shock can form in accretion flow even for super Eddington accretion rate, and can also radiate on or above Eddington luminosity. The efficiency of

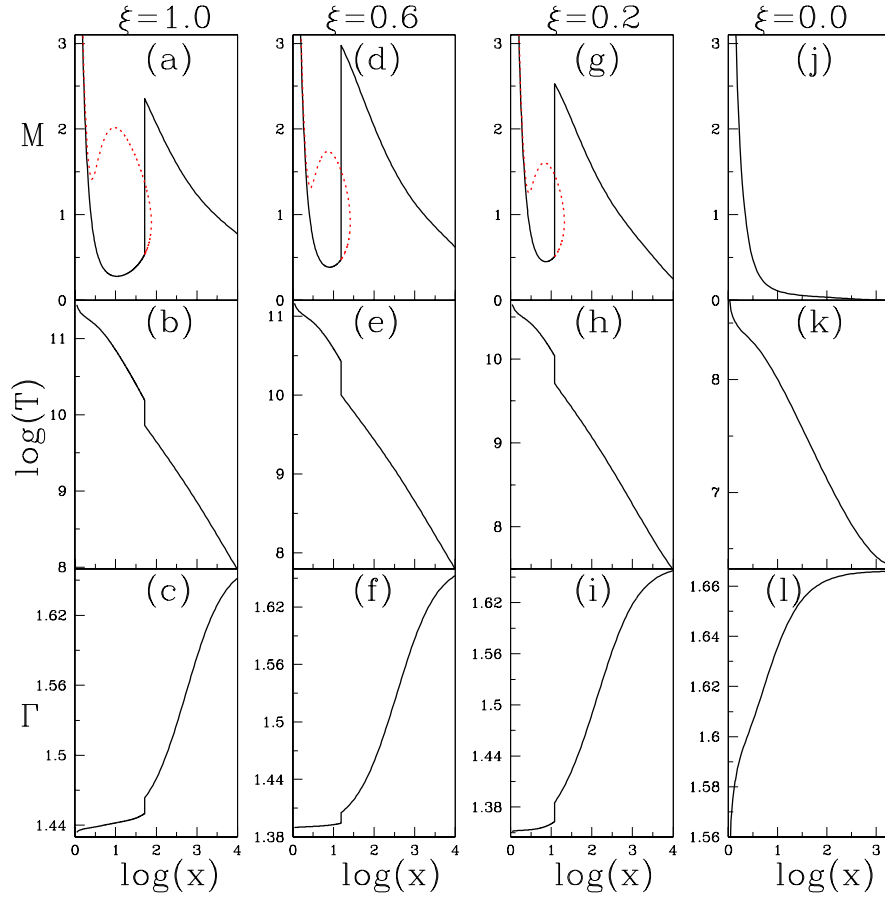


**Figure 10.** Variation of Mach number  $M$  (a, d, g, j),  $\log(T)$  (b, e, h, k) and adiabatic index  $\Gamma$  (c, f, i, l) with radial distance  $\log(x)$ . These solutions are plotted with disc parameters,  $\varepsilon = 1.000001$ ,  $\alpha = 0.01$ ,  $\beta = 0.01$ ,  $\dot{m} = 0.001$  and  $\xi = 1.0$  (a-c),  $0.6$  (d-f),  $0.2$  (g-i),  $0.0$  (j-l). The plots with  $\xi = 1.0, 0.6$ , and  $0.2$  having shock locations at  $x_s = 51.82, 15.43, 12.06$ , respectively. For  $0 \leq \xi \leq 0.157$ , shock solution does not exist for these parameters.

conversion of accretion power to radiation also varies, for example we consider two accretion solutions corresponding to  $\varepsilon = 1.0001$  and  $\alpha = 0.01$ , and  $\lambda_0 = 1.57$  ( $S_1$ ) and  $\lambda_0 = 1.515$  ( $S_2$ ). The dimensionless temperature  $\Theta$  of the two solutions are plotted with  $x$  in log-log scale and are presented in the inset of Fig. 9a.  $S_1$  corresponds to  $\dot{m} = 0.1$  and  $\ell = 2.766 \times 10^{-4}$  and  $S_2$  corresponds to  $\dot{m} = 7$  and  $\ell = 0.677$ . The radiative efficiency defined as  $\ell/\dot{m}$  of  $S_1$  is  $\lesssim 10^{-3}$ , while for  $S_2$  the efficiency is  $\sim 0.1$ . Therefore, the range of radiative efficiency obtained from our solutions, spans from radiatively inefficient advective flow to radiatively luminous regime, and solely depends on the outer boundary conditions. So the cycle of low luminosity to luminous but intermediate hard states in microquasars can be addressed if all the solutions in the advective regime be considered.

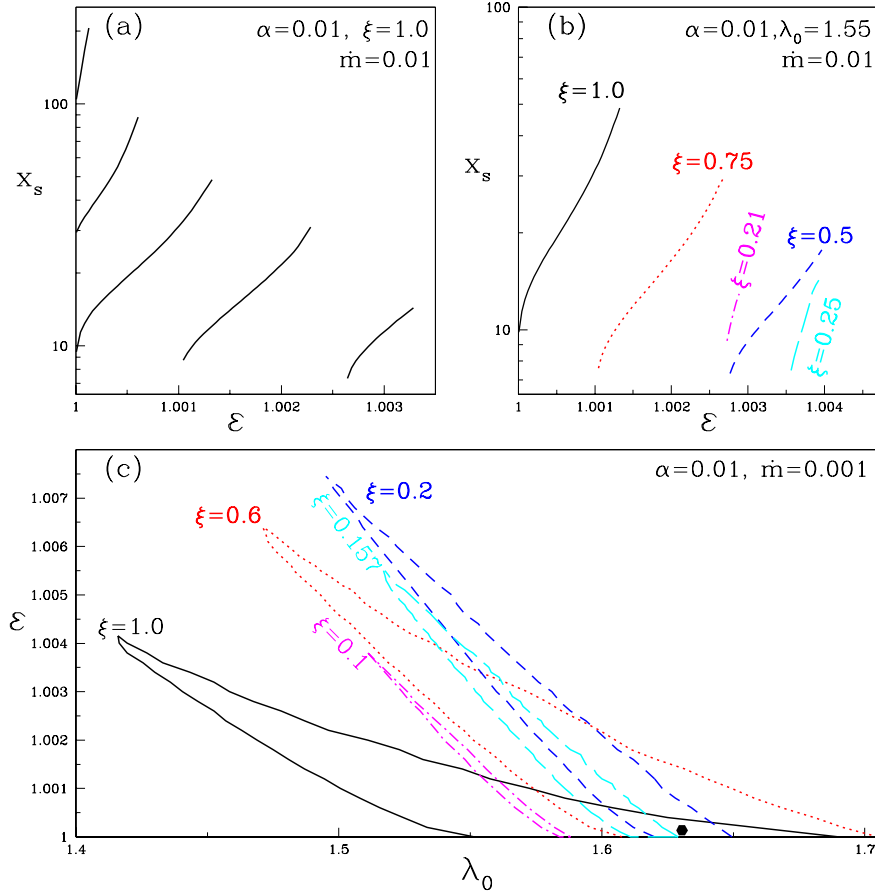


**Figure 11.** (a) Variation of  $\log(x_s)$  with  $\epsilon$ . From left to right, *i.e.*,  $\lambda_0 = 1.65$  to  $1.45$  with decrement  $d\lambda_0 = 0.05$ , with parameters,  $\alpha = 0.01$ ,  $\xi = 1.0$ ,  $\beta = 0.01$ ,  $\dot{m} = 0.01$ , and  $\chi = 1$ . (b) Variation of  $\log(x_s)$  with  $\epsilon$ . The composition of the flow are  $\xi = 1.0$  (solid, online black),  $\xi = 0.75$  (dotted, online red),  $\xi = 0.5$  (dashed, online blue),  $\xi = 0.25$  (long dashed, online cyan),  $\xi = 0.21$  (dashed-dotted, online magenta). Other parameters are  $\alpha = 0.01$ ,  $\lambda_0 = 1.55$ ,  $\beta = 0.01$  and  $\dot{m} = 0.01$ . (c)  $\epsilon - \lambda_0$  parameter space for steady shocks for  $\alpha = 0.01$ ,  $\beta = 0.01$  and  $\dot{m} = 0.001$ . Each curve corresponds to  $\xi = 1.0$  (solid, online black),  $\xi = 0.6$  (dotted, online red),  $\xi = 0.2$  (dashed, online blue),  $\xi = 0.157$  (long dashed, online cyan),  $\xi = 0.1$  (dashed-dotted, online magenta). The black dot near the bottom show the parameters for which solutions of Fig. 10a-10l are plotted.

### 3.2 Effect of composition

All previous figures were for  $e^- - p^+$  flow. In Figs. 10a-10l, we compare flow variables of different  $\xi$ . All the plots are generated for  $\epsilon = 1.000001$ ,  $\lambda_0 = 1.63$ ,  $\alpha = 0.01$ ,  $\beta = 0.01$ , and  $\dot{m} = 0.001$ . We change the composition as we go to the right *i.e.*,  $\xi = 1$  (Figs. 10a-10c),  $\xi = 0.6$  (Figs. 10d-10f),  $\xi = 0.2$  (Figs. 10g-10i) and  $\xi = 0.0$  (Figs. 10j-10l). And we change the flow variable as we go vertically down *i.e.*,  $M$  (Figs. 10a, 10d, 10g, 10j),  $\log(T)$  (Figs. 10b, 10e, 10h, 10k), adiabatic index  $\Gamma$  (Figs. 10c, 10f, 10i, 10l). These solutions correspond to the location marked by the black dot in parameter space shown in Fig. 11c. Once again we show that, like our previous papers (Chattopadhyay 2008; Chattopadhyay & Ryu 2009; Chattopadhyay & Chakrabarti 2011; Chattopadhyay *et al.* 2012; Kumar *et al.* 2013), the temperature of the flow decreases with the decrease of  $\xi$ , but makes the flow thermally more

relativistic (*e.g.*,  $\Gamma_{\xi=1} > \Gamma_{\xi=0.6} > \Gamma_{\xi=0.2}$  in Figs. 10c, 10f, 10i) because of the reduced inertia of the flow over compensates the reduced thermal energy. However, if  $\xi < 0.2$ , the temperature is so low (Fig. 10k) that the reduction in proportion of protons cannot compensate and the reduced temperature of the flow, and it becomes thermally less relativistic ( $\Gamma_{\xi=0} > \Gamma_{\xi \neq 0}$ ). Let us now investigate how the shock location behaves with the variation of  $\varepsilon$  and  $\lambda_0$ . In Fig. 11a, we plot  $\log(x_s)$  with  $\varepsilon$  for parameters  $\alpha = 0.01$ ,  $\xi = 1.0$  and  $\chi = 1$ . From left to right, curves represent  $\lambda_0 = 1.65$  to  $1.45$  with decrement  $d\lambda_0 = 0.05$ . This shows that for a given  $\xi$ , for low  $\varepsilon$  steady state shock will form if  $\lambda$  is high and vice versa. This shows that the accretion shock occurs due to presence of the centrifugal barrier as well as high temperature of the flow. Higher  $\varepsilon$  is symptomatic of hotter flow so it can support steady shocks at lower angular momentum, while flows with lower  $\varepsilon$  needs higher angular momentum to produce shocks. In Fig. 11b, we plot  $\log(x_s)$  with  $\varepsilon$  for parameters  $\alpha = 0.01$ ,  $\lambda_0 = 1.55$ ,  $\beta = 0.01$ ,  $\dot{m} = 0.01$ , and  $\chi = 1$ , but now each curve represent  $\xi = 1.0$  (solid, online black),  $\xi = 0.75$  (dotted, online red),  $\xi = 0.5$  (dashed, online blue),  $\xi = 0.25$  (long dashed, online cyan),  $\xi = 0.21$  (dashed-dotted, online magenta). As  $\xi$  is decreased, the flow becomes more energetic and therefore shock forms at higher  $\varepsilon$ . Since the flow is thermally the most relativistic when  $\xi \sim 0.25$ , so any further decreases in  $\xi$  makes the flow, as well as, the shock to be less energetic, and hence  $x_s$  shifts towards lower  $\varepsilon$ . Similar to the shock location itself, the shock parameter space has a similar tendency. In Fig. 11c, the parameters used for all  $\xi$  are  $\alpha = 0.01$ ,  $\beta = 0.01$  and  $\dot{m} = 0.001$ . The shock parameter space for  $\xi = 1$  (solid, online black) is in the lower  $\varepsilon$ , lower  $\lambda_0$  range, but reduction of protons shifts the shock parameter space to higher  $\varepsilon$  and higher  $\lambda_0$  range ( $\xi = 0.6$  dotted, online red;  $\xi = 0.2$  dashed, online blue). However, further reduction of  $\xi$  makes the flow less energetic and shift towards left ( $\xi = 0.157$  long dashed, online cyan;  $\xi = 0.1$  dashed, online magenta). The black dot show the parameters for which Figs. 10a-10k were generated. For these parameters no shock exist for  $\xi < 0.157$ .

#### 4 DISCUSSION AND CONCLUDING REMARKS

In this paper we presented the solutions of accretion flow in presence of dissipative processes like viscosity and various cooling processes, where the accretion disc fluid is described by variable  $\Gamma$  EoS, and multiple species of particles. As far as we know, such an effort has not been undertaken before in the context of black hole accretion. Presently, we considered only

a Schwarzschild BH. If we had used a Kerr BH, then the length scale would get reduced. The location of the horizon shifts from  $2GM/c^2$  for non-spinning black hole to  $GM/c^2$  for maximally rotating black hole and similarly other locations like marginally stable orbit, marginally bound orbit etc. Since matter enters deeper into the gravitational well for spinning black holes, the accreting matter becomes much hotter than those for non-spinning or slowly spinning black holes. The multiple critical point range of parameter space shifts to higher energy but lower angular momentum part of the parameter space. The counter spinning black holes, on the other hand, makes the flow even colder. However, between maximally counter rotating flow and Kerr parameter of 0.5 co-rotating flow, the difference is not significantly large. For maximally co-rotating flow, the temperature near the horizon is about an order of magnitude higher than that of slowly spinning and non-rotating blackholes. This would lead to much higher radiative efficiency. So the maximum efficiency for non-rotating black holes we got in this paper, was close to 10 % of accretion energy, but the radiative efficiency can go up to 40 % for maximally rotating black hole.

In this paper we have presented the equations of motion in details, identified the constant of motions, and the exact methodology to solve these equations. It is well known, that black hole accretion is transonic, and the location of sonic or critical point and the value of  $\lambda_c$  for a given boundary condition are eigen values of the problem. We obtained the location of the sonic points as eigenvalues, by extending the Frobenius expansion methodology of Becker & Le (2003) to a flow described by variable  $\Gamma$  EoS. Although we were inspired by Becker & Le (2003), to find the asymptotic values of the flow variables close to the horizon, but unlike Becker & Le (2003) we have not used the free fall condition close to the horizon, in order to find the exponents of the series expansion. Rather we used the constants of motion to find them. Consequently, the exponents of the series expansion obtained are different than those obtained by Becker & Le (2003). We have also presented a subsection on shocks, in order to pin point the exact form of the conserved quantities across a thin shock. In the process, we also pointed out that conservation of the Bernoulli parameter or the grand energy, which are constants of motion for inviscid or viscous flow, respectively, becomes a case of dissipative shock when both viscosity and cooling are considered.

We obtained solutions for all possible boundary conditions, and generated shock free smooth solutions, as well as, shocked accretion solutions. We showed that shock free smooth solutions are of two types (i) low  $\lambda$  at the outer boundary or Bondi type solutions with one outer sonic point, and (ii) high  $\lambda$  at the outer boundary, or, ADAF type solutions through

inner sonic point. In Figs. 1, we presented the entire  $\varepsilon - \lambda_0$  parameter space, and all type of solutions possible. We also showed that a Bondi type solution in low  $\lambda_0$ ,  $\alpha$ , and  $\dot{m}$ , may develop multiple sonic points and shocks as we change the boundary condition or change  $\alpha$ ,  $\dot{m}$  etc. But a boundary condition which produces a transonic solution through inner sonic point in the inviscid limit, will not develop a shock for any value of  $\alpha$ ,  $\beta$ , and  $\dot{m}$  (Figs. 2 and 3). We also showed that increasing viscosity or cooling moves the shock closer to the horizon, provided the flow is launched from with the same outer boundary condition (Figs. 5 and 6).

We have considered bremsstrahlung and synchrotron processes as the dominant cooling processes. The inverse Comptonization process has been taken into consideration through a fitting function presented by Kumar *et al.* (2014), where the fitted function is the Compton efficiency for all kind of seed photons (see Kumar *et al.* 2014, for details). We have considered this fitted function as generic, as an obvious effort to simplify things related to Comptonization but nonetheless to incorporate some effects of it in the solution. Since the post shock disc has a jump in temperature and density, it is puffed up, and can hence intercept additional photons from the post shock disc and Comptonize it. A shock free disc has smooth solutions and therefore will not be able to intercept additional photons, reducing the Comptonization efficiency. As a result we found that the shocked disc is more luminous than the shock free disc, even when they start with the same outer boundary condition (Figs. 5a and b). We have shown that shock solutions can be found for high enough viscosity, as well as, very high accretion rates (Figs. 6, 8-9). We have compared the shock parameter space for both non-dissipative shocks and dissipative shocks, and if the total shocked domain in the  $\varepsilon - \lambda_0$  parameter space is considered then it is indeed quite significant. Furthermore Fig. 9 shows a very interesting phenomena in which, for high accretion rate and moderate viscosity parameter values, luminosities of up to and over Eddington limit is possible. This is very interesting, because Fig. 9 show that luminosities of depending on the accretion rate radiatively inefficient and luminous regimes both can be achieved by tuning the matter supply at the outer boundary. Figure 9, further show that luminosities up to  $\ell \sim 10^{39} \text{erg s}^{-1}$  for BHCs of  $M \sim 10M_{\odot}$  *i.e.*, stellar mass black holes, and  $\ell \sim 10^{46} \text{erg s}^{-1}$  for BHCs of  $M \sim 10^8 M_{\odot}$  for super massive black holes can be achieved in advective and shocked accretion domain even when only non-rotating black holes are assumed. This means higher luminosities may be achieved for shocked accretion flow if Kerr black holes are considered. Furthermore, since super-Eddington accretion is possible, then the growth of the central mass also comes into

the ambit of future study. Simple minded estimates show, that a black hole of  $10M_{\odot}$  will increase its mass by 10 % in about 5 Myr, if it continues to accrete at  $10\dot{M}_{\text{Edd}}$ .

One may wonder what difference would it make if fixed  $\Gamma$  equation of state is used. The main difference between solutions obtained by using a correct EoS which produces temperature dependent adiabatic index and a fixed adiabatic index EoS (only correct for low and ultra-relativistic temperatures see Ryu et. al. 2006) is that, the latter either under estimates or over estimates temperature of the flow. A fixed  $\Gamma$  EoS with  $\Gamma = 4/3$  will over estimate the temperature of the flow, and  $\Gamma = 5/3$  will under estimate it all through the flow as was shown by Ryu *et al.* (2006). This would invariably affect the local sound speed, messing up with the location of sonics points. Location and strength of shocks (if it forms) will be affected too, and thereby the radiated power. In the inviscid limit the energy-angular momentum parameter space was compared before (Chattopadhyay 2008), and it showed that the fixed  $\Gamma$  EoS produces too high energies. In other words, when observations would be matched with solutions, we would be predicting wrong temperatures and densities. It is also important to take the composition into account. We have shown that flow with EoS of similar particles ( $\equiv \xi = 0$ ), is physically similar to an  $e^- - e^+$  flow, and is a very low energetic flow with temperatures which are orders of magnitude less than flows composed of baryons and leptons. In other words, a flow described by EoS of similar particle is unlikely to be realized in nature, so for relativistic astrophysical fluid one must study flows using EoS with  $1 \geq \xi > 0$ .

## ACKNOWLEDGMENT

The authors acknowledge the anonymous referee for fruitful suggestions to improve the quality of the paper.

## REFERENCES

- Becker, P. A.; Le, T.; 2003, ApJ, 588, 408
- Becker, P. A., Das, S., Le, T., 2008, ApJ, 677, L93
- Biretta J. A., 1993, in Burgerella D., Livio M., Oea C., eds, Space Telesc. Sci. Symp. Ser., Vol. 6, Astrophysical Jets. Cambridge Univ. Press, Cambridge, p. 263
- Blumenthal, G. R. & Mathews, W. G. 1976, ApJ, 203, 714.
- Bondi, H.; 1952, MNRAS, 112, 195

- Chakrabarti S.K., ApJ, 1989, 347, 365
- Chakrabarti, S K., Titarchuk, L., 1995, ApJ, 455, 623.
- Chakrabarti S.K., 1996, ApJ, 464, 664
- Chattopadhyay, I.; Das, S., 2007, New A, 12, 454
- Chattopadhyay, I., 2008, in Chakrabarti S. K., Majumdar A. S., eds, AIP Conf. Ser. Vol. 1053, Proc. 2nd Kolkata Conf. on Observational Evidence of Black Holes in the Universe and the Satellite Meeting on Black Holes Neutron Stars and Gamma-Ray Bursts. Am. Inst. Phys., New York, p. 353
- Chattopadhyay I., Ryu D., 2009, ApJ, 694, 492
- Chattopadhyay I., Chakrabarti S.K., 2011, Int. Journ. Mod. Phys. D, 20, 1597
- Chattopadhyay, I.; Mandal, S.; Ghosh, H.; Garain, S.; Kumar, R.; Ryu, D. , 2012, BASI, ASI Conf. Ser. Vol. 5, pp 81-89
- Das S., Chattopadhyay I., Nandi A., Chakrabarti S.K., 2001, A&A, 379, 683
- Das, S., 2007, MNRAS, 376, 1659
- Das, S.; Chattopadhyay, I., 2008, New A, 13, 549.
- Das, S., Chattopadhyay, I., Nandi, A., Molteni, D., 2014, MNRAS, 442, 251.
- Doeleman S. S. et al., 2012, Science, 338, 355.
- Fukue, J., 1987, PASJ, 39, 309
- Gallo, E., Fender, R. P., Pooley, G., G., 2003 MNRAS, 344, 60
- Giri, K., Chakrabarti, S. K., 2013, MNRAS, 430, 2826
- Gu, Wei-Min; Lu, Ju-Fu; 2004, ChPhL, 21, 2551
- Junor W., Biretta J.A., Livio M., 1999, Nature, 401, 891
- Kumar R., Chattopadhyay I., 2013, MNRAS, 430, 386
- Kumar, R.; Singh, C. B.; Chattopadhyay, I.; Chakrabarti, S. K.; 2013, MNRAS, 436, 2864
- Kumar, R.; Chattopadhyay, I.; Mandal, S.; 2014, MNRAS, 437, 2992, 147
- Landau, L. D., Lifshitz, E. M., 1959, Fluid Mechanics, Course of theoretical physics, Oxford: Pergamon Press.
- Lanzafame, G., Molteni, D., Chakrabarti, S. K., 1998, MNRAS, 299, 799
- Lanzafame, G., Cassaro, P., Schilliró, F., Costa, V., Belvedere, G., Zapalla, R. A., 2008, A&A, 473, 482
- Lee, Seong-Jae; Ryu, Dongsu; Chattopadhyay, Indranil; 2011, ApJ, 728, 142
- Liang, E. P. T., Thompson, K. A., 1980, ApJ, 240, 271L
- Lu, J. F., Gu, W. M., & Yuan, F. 1999, ApJ, 523, 340



- McHardy I. M., Koerding E., Knigge C., Fender R. P., 2006, *Nature*, 444, 730
- Michel, F. C., 1972, *Ap&SS*, 15, 153
- Mirabel I. F., Rodriguez L. F., 1994, *Nature*, 371, 46
- Molteni, D., Lanzafame, G., Chakrabarti, S. K., 1994, *ApJ*, 425, 161
- Molteni, D., Sponholz, H., Chakrabarti, S. K., 1996a, *ApJ*, 457, 805
- Molteni, D., Ryu, D., Chakrabarti, S. K., 1996b, *ApJ*, 470, 460
- Mukhopadhyay, B., Dutta, P., *New A.*, 17, 51
- Nandi, A., Debnath, D., Mandal, S., Chakrabarti, S. K., 2012, *A&A*, 542A, 56.
- Narayan, R., Kato, S., Honma, F., 1997, *ApJ*, 476, 49
- Nagakura, H., Yamada, S., 2009, *ApJ*, 696, 2026
- Novikov, I. D.; Thorne, K. S., 1973, in Dewitt B. S., Dewitt C., eds, *Black Holes*. Gordon & Breach, New York, p. 343
- Paczynski, B. and Wiita, P.J., 1980, *A&A*, 88, 23.
- Rybicki, G. B., Lightman, A. P., 1979, *Radiative Processes in Astrophysics*, Wiley-Interscience Publication, New York.
- Remillard R.A., McClintock J.E., 2006, *ARA&A*, 44, 49
- Ryu, D., Chattopadhyay I., Choi E., 2006, *ApJS*, 166, 410
- Shakura, N. I., Sunyaev, R. A., 1973, *A&A*, 24, 337S.
- Shaposhnikov N., Titarchuk L., 2009, *ApJ*, 699, 453
- Shapiro, S. L., 1973, *ApJ*, 180, 531
- Shapiro S. L., Teukolsky S. A., 1983, *Black Holes, White Dwarfs, and Neutron Stars: The Physics of Compact Objects*. Wiley-Interscience, New York
- Smith, D. M., Heindl, W. A., Marckwardt, C. B., Swank, J. H., 2001, *ApJ*, 554 L41.
- Smith, D. M., Heindl, W. A., Swank, J. H., 2002, *ApJ*, 569, 362.
- Smith, D. M., Dawson, D. M., Swank, J. H., 2007, *ApJ*, 669, 1138.
- Sunyaev, R. A.; Titarchuk, L. G.; 1980, *A&A*, 86, 121
- Svensson, R.; 1982, *ApJ*, 258, 335
- Taub A.H., 1948, *Phys. Rev.*, 74, 328
- Weinberg, S.; 1972, *Gravitation and Cosmology: Principles and Applications of the General Theory of Relativity*, John Wily & Sons, New York.